FIRST PRINCIPLE STUDY OF Ti-Al AND Pt-Ti ALLOYS

by

ROSINAH MAHLANGU

RESEARCH DISSERTATION

Submitted in fulfillment of the requirements for the degree of

MASTER OF SCIENCE

in

Physics

in the

FACULTY OF SCIENCES & AGRICULTURE

(School of Physical & Mineral Sciences)

at the

UNIVERSITY OF LIMPOPO (Turfloop Campus)

SUPERVISOR: Prof. P.E. Ngoepe

CO- SUPERVISORS: Mr. M.J. Phasha

: Dr. H.R. Chauke

2009

Abstract

The structural and energetic properties of the Ti-Al and Pt-Ti alloys have been carried out using first-principles total energy calculation of the density functional theory. We found a good correlation between VASP and CASTEP calculations with the experimental data. The equilibrium lattice constants for both systems are in good agreement with the experimental values (within 3% agreement). Furthermore, the heats of formation were calculated in order to determine the relative structural stabilities of the Ti-Al and Pt-Ti alloys. We predict that the $L1_0$ TiAl is the most stable structure with the lowest heats of formation (more negative ΔH_f) consistent with the experimental observations. The 50% composition of the PtTi SMA's in particular B19/B19′ phases predict values to be closer to each other, with B19′ being the most stable phase. A comparison of the energy differences between different PtTi phases, yields the relative energies in the order B2>$L1_0$>B19>B19'. The elastic constants for B19/B19′ and $L1_0$ show the positive shear modulus while a negative shear modulus was observed for B2 phase (mechanical instability). Similarly, the phonon dispersions and the density of states for the B2, $L1_0$, B19 and B19′ PtTi shape memory alloys were calculated and are consistent with the heats of formation. The phonon dispersion curves revealed a softening of modes along high symmetry directions (M and R). This confirms that the B2 structure is less stable as compared to the other structures. The density of states for the 50% PtTi composition structures were also calculated and are consistent with the stability trend. Furthermore the transformation from B2-$L1_0$ was investigated using Bain's path and the B2 and $L1_0$ phases were depicted at c/a=1 and c/a=$\sqrt{2}$ respectively.

Declaration

I declare that the dissertation hereby submitted to the University of Limpopo (Turfloop Campus) for the degree of Master of Science has not previously been submitted by me for a degree at this or any other university, that it is my own work both in design and execution, and that all material contained herein has been duly acknowledged.

Ms R. Mahlangu _____

Student Number: 9817624 **Date**

Dedications

This work is dedicated to my lovely daughters, Simphiwe and Lehlogonolo, my parents Mahlosi and Pulane Mahlangu, my sisters Mapula, Masesi, Jabulile and my brother Sipho. To my uncles, Mayedwa and Mandlakayise thank you for all the support you have given me during my years of study. Granny Mantlhanyane Mohlamonyane, you stood by me through all and gave me the reason to look into the future. Wherever you are, this is for you, may your soul rest in peace.

Acknowledgements

Foremost, I would like to thank my supervisor, Prof. P.E. Ngoepe, who has shared with me a lot of his expertise and research insight. He quickly became for me the role model of a successful researcher in the field. I also like to express my gratitude to M.J. Phasha and Dr H.R. Chauke, who's thoughtful, advises often served to give me a sense of direction during this study. And I am deeply grateful to the NRF and CSIR for the financial support that they gave me in order to study MSc.

Above all I would like to thank the almighty God for all the strength and perseverance he has installed in me during all the years of my studies, without him this work wouldn't have been started. I wish to thank everybody with whom I have shared experiences in life. From the people who first persuaded and got me interested into the study of computational modelling, especially those who also played a significant role in my life, to those which with the gift of their company made my days more enjoyable and worth living. I can be punished if I don't make mention of the people who helped me with their useful input in this work, MMC members, thank you.

I cannot finish without saying how grateful I am with my family: grandparents, uncles, aunts, cousins and nephews all have given me a loving environment where to develop. Particular thanks, of course, to my mother Pulane, Mapula my sister and best mates. They have always supported and encouraged me to do my best in all matters of life. To

Benedict, Simphiwe and Lehlogonolo, thank you for the support and love you have given me through all this study.

Table of contents

List of figures

List of tables

Chapter 1

Introduction

In this chapter we give a brief review of the previous theoretical and experimental studies on titanium aluminium (Ti-Al) and platinum titanium (Pt-Ti) shape memory (SMA's) alloys. The importance of the platinum mineral groups, are briefly summarized and lastly the objectives and outline of the current work are given.

1.1. Background

Over the last decades, there has been a significant increase in the use of light metals such as aluminium (Al), magnesium (Mg), titanium (Ti), lithium (Li) and precious metals such as platinum (Pt). Amongst these metals, titanium as a transition metal is a lightweight, silver-grey material with atomic number of 22 and atomic weight of 47.90. It has a density of 4510 kg/m^3, an excellent corrosion resistance and a high strength to weight ratio. However, Mg is the eighth lightest metal with density of 1738 kg/m^3 whereas platinum on the other hand is a beautiful silvery-white metal when pure and is malleable and ductile with a density of 21090 kg/m^3 [1].

1.1.1. Ti-Al alloys

Intermetallics involving Al and early transition metals (TM) are known to have many attractive properties, making them desirable candidates for high temperature structural

applications [2, 3]. Properties include resistance to oxidation and corrosion, elevated temperature strength, relative low density and high melting point. They have received particular interest as the basis for advanced engineering materials. However, these alloys have low ductility and toughness at ambient temperature and are difficult to process by conventional processing routes [4, 5].

In the past years there have been significant advances in the fundamental understanding of both mechanical properties and phase stability of intermetallics provided by the results of quantum mechanical electronic structure calculations. Ab initio methods based on density functional theory have been used to derive heats of formation and the relative stability of competing structures [6, 7]. Many of ab initio studies in Ti-Al systems have been devoted to understanding the properties of monolithic intermetallics of particular structure. In order to design multicomponent and multiphase materials it is necessary to model the relative stability of all competing phases. To understand processing microstructure property performance links in multicomponent and multiphase materials, a frame work is needed to address the dynamics of microstructure evolution [8]. In this work we investigate the zero temperature energetics and the equilibrium lattice properties of Ti-Al intermetallics using ab initio computational techniques.

1.1.2. Pt-Ti shape memory alloys

Since the discovery of shape memory effect (SME) the attention of researchers has been turned to binary transition metal alloys, which exhibit a martensitic phase transform accompanied by SME. Shape memory bulk Ti-based alloys such as NiTi, PdTi, AuTi and

PtTi have been the subject of intensive experimental and theoretical investigations [9]. Amongst these, the useful martensitic transformation temperatures (T_m) of NiTi alloys are around ±100°C, similar to those of diverse copper based SMA's [10].

Owing to their unique properties, they have attracted significant interest in various industries. The T_m of AuTi and PdTi are in the range from 400°C to 600°C, depending on the stoichiometry [11]. However, the T_m of PtTi is much higher, at approximately 1000°C [4] and this is considered to be of potential technological interest for elevated temperature SMA applications. It also undergoes a B2-B19 martensite phase transformation with a transition temperature of approximately 1050°C [11, 12, 13, 14] as shown in figure 1.1.

Furthermore, titanium and its alloys, owing to their high strength to weight ratio and high temperature properties, are used extensively by the aerospace industry. They are typically utilized for airplane parts and fasteners. The same properties make them useful for the production of gas turbine engines, particularly for parts such as the compressor blades, casings, engine cowlings and heat shields.

In addition, PtTi is more promising as a very high temperature shape memory alloy system since Pt has high temperature advantages over nickel (Ni), palladium (Pd) and gold (Au). Pt melting point is higher than that of Ni, Pd and Au (e.g. Pt melting point is 1768 °C, Ni= 1455°C, Pd= 1555°C and Au= 1064°C) and therefore could be used at higher temperatures. However, not much has been done to understand the shape-memory

behaviour of the binary alloys, though limited mechanical properties have been determined for some ternary systems.

The transformation from B2 to B19 PtTi has been investigated in the recent work; however, the overwhelming interest by industry is focused on their pressure dependent properties. Nishimura and Hiramatsu [15] undertook the most comprehensive study of the Pt-Ti phase diagram, using metallography, X-ray analysis and differential thermal analysis (DTA). Shape memory effect in Pt-Ti system is so far achievable within 50-50 composition range.

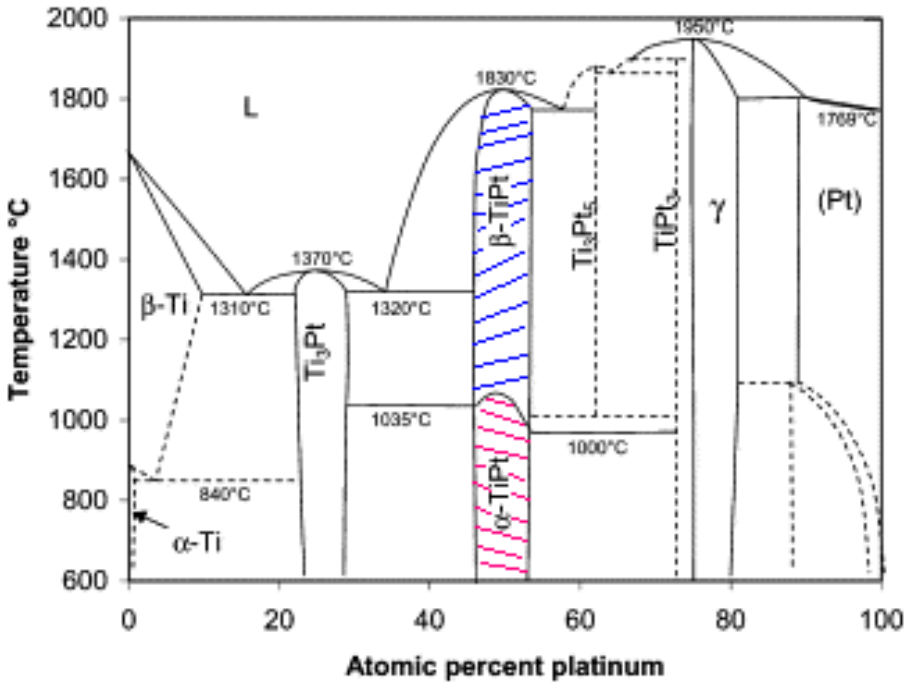

Figure 1-1. The binary phase diagram of Pt-Ti alloys [16].

Shape memory alloys are in general metals that recover from up to 10% deformation via stress and temperature-induced phase transformation. They undergo martensitic transformations, which are displacive transformations dominated by shear distortions of the crystal lattice [17]. Transformation occurs between solid phases, termed the martensite and austenite phases. In general, martensite is the material phase that is stable at low temperatures relative to austenite, which is stable at high temperatures. Further investigation of the mechanical and elastic properties is necessary for determining the shear, bulk and Young's moduli of the Pt-Ti alloy systems.

1.2. The 50% composition of the PtTi SMA's

In this work we will focus mainly on the 50% composition of the PtTi structures i.e. B2, $L1_0$, B19/B19′ as shown in figure 1.2. B2 is a cubic high temperature structure with the space group Pm3-m. The positions of the atoms are shown in Table 1.1 and it is denoted by the pearson symbol cP2. Its experimental lattice parameter is a=4.120Å [18] and its prototype is CsCl.

The low temperature structure B19 is an orthorhombic having the spacegroup Pmma with experimental lattice parameters a=4.764, b=3.154, c=4.864Å [19]. The pearson symbol of B19 is oP4. B19 has a prototype of AuCd with all angles being 90. There is a similarity in the positions of the atoms of the B19 and B19′ as shown in Table 1.2. The B19′ structure is a monoclinic with the spacegroup $Pm/2_1$

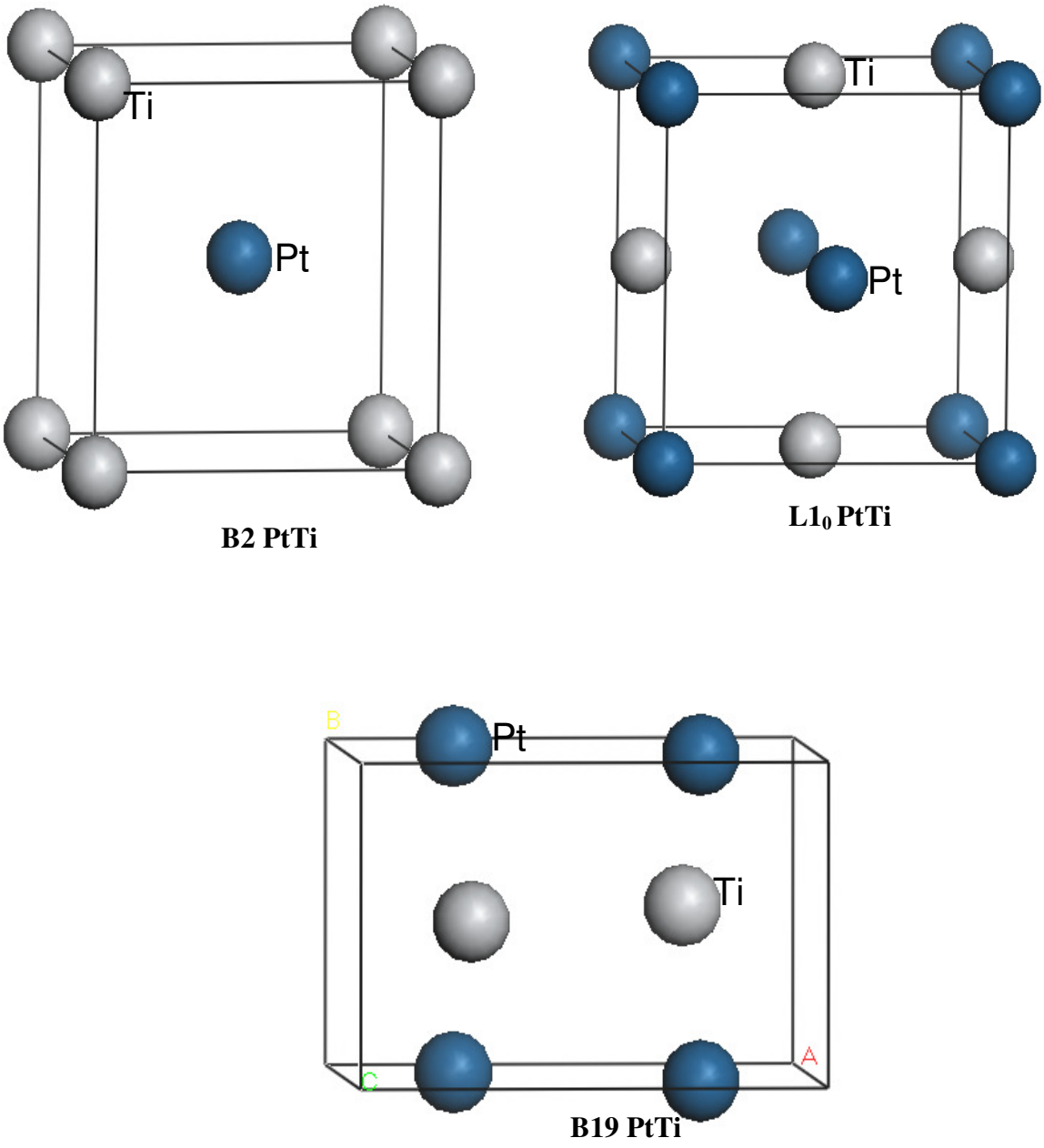

Figure 1-2. The B2, $L1_0$ and B19 PtTi structures

$L1_0$ is an fcc structure having the spacegroup P4/mmm. The experimental lattice parameters are a=2.815, c=3.170Å [20], with the pearson symbol of tP2. The prototype of $L1_0$ is AuCu. The positions of the atoms are shown in Table 1.3.

1.3. Background on the properties to be investigated

First principle calculations refer to an approach where properties of materials i.e. structural, electronic, optical, etc can be determined using quantum mechanical methods. Some of the properties including heats of formation, elastic properties, phonon dispersions and the density of states will be reviewed below as they are appropriate for the current study. The phonon dispersions and the density of states will be reviewed as they are appropriate for the current study.

1.3.1. Heats of formation

It has become quite commonplace for electronic structural calculations, of varying rigor, to yield the total energy of a solid. This offers a prospect of estimating the stabilities of phases which are either unavailable or inaccessible experimentally and this, in turn, has implications for making phase diagram predictions. Heats of formation from ab initio calculations have been successfully used to predict the stability of alloys and in construction of their phase diagrams [21, 22, 23, 24, 25]. Nguyen-Manh et al [26] also performed calculations on the heats of formation for the 4d transition metal aluminides with respect to 12 different AB-structure types. In this work we will use the heats of formation to predict the stability of the Ti-Al and Pt-Ti alloy for different phases.

Table 1-1. The atomic positions (Wyckoff notation) in the B2 PtTi crystal structure

Structure	Atom	Positions	x	y	z
B2	Ti1	1a	0.000	0.000	0.000
	Pt1	1b	0.500	0.500	0.500

Table 1-2. The atomic positions (Wyckoff notation) in the B19 PtTi crystal structure

Structure	Atom	Positions	x	y	z
B19	Ti1	2f	0.250	0.500	0.812
	Pt1	2e	0.250	0.000	0.321

.

Table 1-3. The atomic positions (Wyckoff notation) in the $L1_0$ PtTi crystal structure

Structure	Atom	Positions	x	y	z
$L1_0$	Ti1	1a	0.000	0.000	0.000
	Pt1	1b	0.177	0.177	0.134

1.3.2. Elastic constants

Ab initio calculations for the determination of elastic constants are more complex than the calculations of bulk properties (i.e. lattice constants, heats of formation, etc.). The application of strain on the lattice implies a lowering of symmetry from that of bulk crystal and the strain energy involved is small.

Nguyen-Manh et al [26] calculated the elastic constants of transition metal aluminide intermetallics for the ground-state structures e.g. TiAl, FeAl, CoAl, etc. The other work reported was the calculations of the elastic constant on Co/Pt superalloys [27] and SiO_2 and $MgAl_2O_4$ [28] using ab initio methods. The problem of ductile versus brittle response of crystals requires the fracture strength in addition to their deformability. Pugh [29] introduced the quotient of bulk modulus to shear modulus, B/C' as an indication of the extent of fracture range in metals. A high value of B/G is associated with ductility and a low value with brittleness. In this study we note that the lowest heat of formation is associated with ductility whereas the highest value is associated with the brittleness of the structure. This stipulates the relationship between the heat of formations and the elastic constants in terms of stability.

1.3.3. Phonon dispersions

The phonon spectrum of a solid is important in evaluating physical quantities such as specific heat, thermal expansion coefficient and electron-phonon interactions [30]. With the advent of computational techniques, calculations of phonon frequencies within the local density approximation (LDA) became possible [31, 32, 33, 34]. Palacios et al [35]

also calculated the phonon dispersion of $Ti_xGa_nAs_m$ and $Ti_xGa_nP_m$ using the ab initio method.

The phonon spectra and effective charges of the group-IV semiconductors (Si and Ge diamond structure) and of the zinc-blende structure III-V semiconductors GaAs, GaSb, AlAs and AlSb were calculated by Giannozzi *et al.* [36]. Chauke *et al* [22] also successfully calculated the phonon dispersion of the Pt_3Al alloys on the $L1_2$, DO'_c and tP16 phases using the VASP code to compare their stabilities. There is also a recent work reported by Stewart et al [37] on the investigation of phonon dispersion and anomalies in Pd. In this work we will calculate the phonon dispersion of the 50% composition of PtTi to compare their stabilities.

1.3.4. Electronic density of states

Similarly the heats of formation, elastic constants and phonon dispersion, density of states (DOS) can be used to predict the stability of metal alloys. There is experimental evidence that links the electronic structure to the stability for a broad class of Ti-based shape memory alloys [38, 39]. This can be observed where the Fermi level hits the pseudogap of the density of states plot. Rajagopalan and Sundareswari et al [40] calculated the density of states of rhodium based intermetallics and Ghosh et al [41] also did calculations of density of states on the FePd and $FePd_3$ intermetallics the results were in good agreement with the experiment.

1.4. Objectives

In this thesis we investigate the Ti-Al and Pt-Ti alloys, in particular the PtTi structures using the first principles density functional theory (DFT) [42, 43].

Furthermore we determine the equilibrium lattice parameters and the heats of formation of the Ti-Al and Pt-Ti alloys. The results are compared with the available experimental data in order to validate the methodologies employed in the current study. We are more interested in the 50% composition of the Pt-Ti shape memory alloys. We will investigate the stability of the structures at that composition and deduce the most stable phase by comparing their heats of formation.

The electronic and elastic properties of the B19 PtTi system have been investigated and are well reproduced by density-functional theory calculations assuming the experimentally determined structure [44-46]. In this work we will perform the elastic and electronic properties of the B19, B19′, B2 and $L1_0$ and compare the results with the available experimental and calculated results. We will also apply pressure to the 50% composition structures and observe how the structural stabilities change. Furthermore, we will use the equation of states to determine the bulk moduli of interested composition and compare the results with the directly calculated elastic constants.

Lastly, we will investigate the stability of PtTi from first principle calculations of phonon dispersion frequencies, drawing on the strong analogy between B2, $L1_0$, B19′ and B19 transformations. A detailed comparison of the calculated results will be presented.

1.5. Outline

In Chapter 1, we delt with the literature review of the Ti-Al and Pt-Ti alloys. We briefly summarised the importance and uses of these alloys,what has been achieved previously in both experimental and computational approaches. In Chapter 2 we discuss the theoretical techniques that will be used in performing the calculations of the Ti-Al and Pt-Ti systems. The density functional theory and planewave pseudopotential methods are summarised. In Chapter 3 we present the results generated in this study. We will discuss the equilibrium lattice parameters and the heats of formation, comparing them with the available experimental results. In Chapter 4 we discuss the mechanical properties, phonon dispersion and the density of states for the 50% composition of the PtTi shape memory alloys. Finally in Chapter 5 we give the summary of the results.

Chapter 2

Theoretical techniques

2.1. Introduction

We will be using computer simulation techniques which offers an alternative way of investigating properties of materials (using computers), whereby the simulator builds a model of a real system and explores its behaviour. The mathematical model is physically based with the exploration being done on a computer. In many ways these simulation studies share the same mentality as experimental investigations. However, in a simulation there is absolute control and access to detail and given enough computer power, exact answers for the model. The commonly known computational technique is based on ab initio method.

Ab initio is a group of methods in which properties of materials i.e. the values of the fundamental constants and the atomic numbers of the atoms present can be calculated using Schrödinger equation. These methods include density functional theory (DFT), Hartree-Fock (HF) methods and post-Hartree-Fock (PHF) methods. In the current study, we will only focus on the density functional theory for predicting the ground-state energy of many-body system.

Several factors have contributed to the present success of ab initio calculations for real materials systems. The first is the availability of modern high speed computers. This has made it possible to carry out calculations on real materials in interesting situations with sufficient accuracy that there can be meaningful detailed comparison with experimental measurements. The second is the advent of density functional theory (DFT) and continuing development of approximations to the DFT formalism for electron exchange and correlation. The third is the refinement in band structure calculation techniques and the invention of the *ab initio* pseudopotentials [47], which have led to rapid computation of total energies. The density functional method has made it feasible to calculate the ground state energy and charge density with remarkably accurate results for real solids. This is the starting point for almost all current first-principle calculations of total energies of solids. Finally, there have been significant new developments in experimental techniques and materials preparation that are making it possible to probe the structure of matter in ways which were never realized before. One advance is the ability to create high pressures and explore the properties of matter over a wide range of densities [48]. This is an ideal experimental tool to provide information that can be compared directly with current theoretical calculations.

2.2. Density functional theory

Density functional theory (DFT) was formulated by Hohenberg and Kohn [42] and Kohn and Sham [43] in the 1960's to provide the foundation for accurate calculations. In DFT, the total electron density is decomposed into one-electron densities,

$$E = E[\rho] \tag{2-1}$$

which are constructed from one-electron wavefunctions.

The idea of using the electron density as the fundamental entity of a quantum mechanical theory of matter originates in the early days of quantum mechanics in the 1920's, especially by the work of Thomas [49] and Fermi [50]. However, in the subsequent decades, it was rather the Hartree-Fock approach [51, 52], which was developed and applied to small molecular systems. Calculations on realistic solid state systems were then out of reach. In 1951, Slater [53] used ideas from the electron gas with the intention to simplify Hartree-Fock theory to a point where electronic structure calculations on solids became feasible. Slater's work, which led to the so-called $X\alpha$ method [54], has contributed tremendously to the development of electronic structure calculations. In solid-state systems, molecules and atoms, the electron density is a scalar function defined at each point *r* in real space,

$$\rho = \rho(\mathrm{r}). \tag{2-2}$$

The electron density and the total energy depend on the type and arrangements of the atomic nuclei. Therefore, one can write

$$E = E[\rho(r), \{R_\alpha\}] \tag{2-3}$$

where the set $\{R_\alpha\}$ denotes the positions of all atoms, α, in the system under consideration. Equation (2-3) is the key to the atomic-scale understanding of electronic, structural and dynamic properties of matter. If one has a way of evaluating expression (2-3), one can, for example, predict the equilibrium structure of solid, one can predict the reconstruction of surfaces and the equilibrium geometry of molecules adsorbed on

surfaces. Furthermore, the derivative of the total energy (2-3) with respect to the nuclear position of an atom gives the force acting on that atom. This enables the efficient search for stable structures and, perhaps more importantly, the study of dynamical processes such as diffusion or the reaction of molecules on surfaces. Most of the considerations discussed here are based on the Born-Oppenheimer approximation in which it is assumed that the motions of the electrons are infinitely faster than those of the nuclei. In practice this means that the electronic structure is calculated for a fixed atomic arrangement and the atoms are then moved according to classical mechanics. This is a fairly good approximation for heavy atoms like tungsten (W), but may cause errors for light atoms such as hydrogen (H) or lithium (Li).

In density functional theory, the total energy (2-1) is decomposed into three contributions, a kinetic energy and a Coulomb energy due to classical electrostatic interactions among all charged particles in the system and a term called the exchange-correlation energy that captures all many-body interactions,

$$E = T_0 + U + E_{xc}\,. \tag{2-4}$$

The most straightforward term is the Coulomb energy *U*. It is purely classical and contains the electrostatic energy arising from the Coulomb attraction between electrons and nuclei, the repulsion between all electronic charges and the repulsion between nuclei

$$U = U_{en} + U_{ee} + U_{nn} \quad , \tag{2-5}$$

with

$$U_{en} = -e^2 \sum_{\alpha} Z_{\alpha} \int \frac{\rho(r)}{|r - R_{\alpha}|} dr \quad , \tag{2-6}$$

$$U_{ee} = e^2 \iint \frac{\rho(r)\rho(r')}{|r - r'|} dr dr' \quad , \tag{2-7}$$

$$U_{nn} = e^2 \sum_{\alpha\alpha'} \frac{Z_\alpha Z_{\alpha'}}{|R_\alpha - R_{\alpha'}|} \quad , \tag{2-8}$$

where e is the elementary charge of a proton and Z_α is the atomic number of atom α. The summations extend over all atoms and the integrations over all space. Once the electron density and the atomic numbers and positions of all atoms are known, expression (2-6) to (2-8) can be evaluated by using the techniques of classical electrostatics.

The kinetic energy term, T_0, is more subtle. In density functional theory, the "real" electrons of a system are replaced by "effective" electrons with the same charge, mass and density distribution. However, effective electrons move as independent particles in an effective potential, whereas the motion of a "real" electron is correlated with those of all other electrons. T_0 is the sum of the kinetic energies of all effective electrons moving as independent particles. Often, one does not explicitly make this distinction between real and effective electrons.

If each effective electron is described by a single particle wave function, ψ_i, then the kinetic energy of all effective electrons in the system is given by

$$T_0 = \sum n_i \int \psi_i^*(r) \left[-\frac{\hbar^2}{2m} \nabla^2 \right] \psi_i(r) dr \quad . \tag{2-9}$$

Expression (9) is the sum of the expectation values of one-particle kinetic energies; n_i denotes the number of electrons in state *i*. By construction, dynamical correlations between the electrons are excluded from T_0.

The third term of Eq. (2-5), called exchange-correlation energy, E_{xc}, includes all remaining complicated electronic contributions to the total energy. The Hohenberg-Kohn-Sham theorem, which is a central part of density functional theory, states that the total energy is at its minimum value for the ground state density and that the total energy is stationary with respect to first-order variations in the density, i.e.

$$\frac{\partial E[\rho]}{\partial \rho}\Big|_{\rho=\rho_0} = 0 \qquad . \tag{2-10}$$

In conjunction with the kinetic energy, we have introduced one-particle wavefunctions $\psi_i(r)$, which generate the electron density

$$\rho(r) = \sum_i n_i |\psi_i(r)|^2 \tag{2-11}$$

where n_i denotes the occupation number of the eigenstate *i*, which is represented by the one-particle wave function ψ_i. By construction, $\rho(r)$ in Eq. (2-11) is the exact many-electron density.

The goal of the next step is the derivation of equations that can be used for practical density functional calculations. The variational condition (2-10) can be used to derive the conditions for the one-particle wavefunctions that lead to the ground state density. To this

end, one substitutes Eq. (2-11) in expression (2-10) and varies the total energy with respect to each wave function. This procedure leads to the following equations:

$$\left[-\frac{\hbar^2}{2m}\nabla^2 + V_{eff}(r)\right]\psi_i(r) = \varepsilon_i\psi_i(r) \quad , \tag{2-12a}$$

with

$$V_{eff}(r) = V_C(r) + \mu_{xc}[\rho(r)] \quad . \tag{2-12b}$$

Equations (2-12) are called the Kohn-Sham equations. The electron density, which corresponds to these wavefunctions, is the ground state density which minimizes the total energy.

As a consequence of the partitioning of the total energy (2-4), the Hamiltonian operator in the Kohn-Sham equations (2-12) contains three terms, one for the kinetic energy, the second for the Coulomb potential and the third for the exchange-correlation potential.

The kinetic energy term is the standard second-order differential operator of one-particle Schrödinger equations and its construction does not require specific knowledge of a system. In contrast, the Coulomb potential operator, $V_C(r)$ and the exchange-correlation potential operator, μ_{xc}, depend on the specific electron distribution in the system under consideration.

The Coulomb or electrostatic potential $V_C(r)$ at point r is generated from the electric charges of all nuclei and electrons in the system. It can be evaluated directly in real space,

$$V_C(r) = -e^2\sum_\alpha \frac{Z_\alpha}{|r - R_\alpha|} + e^2\int \frac{\rho(r')}{|r - r'|}dr' \quad . \tag{2-13}$$

In condensed systems it is more convenient to use Poisson's equation

$$\nabla^2 V_C(r) = -4\pi e^2 q(r) \tag{2-14}$$

to calculate the electrostatic potential. Here, $q(r)$ denotes both the electronic charge distribution $\rho(r)$ and the positive point charges of the nuclei at positions R_α.

The exchange-correlation potential is related to the exchange-correlation energy by

$$\mu_{xc}(r) = \frac{\partial E_{xc}[\rho(r)]}{\partial \rho(r)} \tag{2-15}$$

Equation (2-15) is formally exact in the sense that it does not contain any approximations to the complete many-body interactions.

Therefore, from the above discussions, the Kohn-Sham total energy functional can be expressed as

$$E = \frac{1}{2}\sum_{occ} \varepsilon_i + U_{nn} - \frac{e^2}{2}\iint \frac{\rho(r)\rho(r')}{|r-r'|} dr dr' + E_{xc}[\rho(r)] - \int \rho(r)\mu_{xc} dr$$

In practice however, the exchange-correlation energy (and thus the exchange-correlation potential) is not known and one has to make approximations which will be discussed in the next section.

2.3. Approximation methods

2.3.1. Local density approximation

Several different schemes have been developed for obtaining approximate forms for the functional; for the exchange-correlation energy. The simplest accurate approximation, for non-magnetic systems is to assume that the exchange-correlation energy is dependent

only on the local electron density d(r) around each volume element. Local density approximation (LDA) gives the correct sum rule for the exchange correlation hole [55-57].

In the local density approximation given by

$$E_{xc}[\rho] \approx \int \rho(r)\varepsilon_{xc}^{0}[\rho(r)]dr \qquad (2\text{-}16)$$

the exchange-correlation energy is taken from the known results of the many-electron interactions in an electron system of constant density (homogeneous electron gas). The LDA amounts to the following picture: at each point in a molecule or solid there exists a well defined electron density; it is assumed that an electron at such a point experiences the same many-body response by the surrounding electrons as if the density of these surrounding electrons had the same value throughout the entire space as at the point of the reference electron. The exchange-correlation energy of the total molecule or solid is then the integral over the contributions from each volume element.

A large number of total energy calculations have shown that the LDA gives interatomic bond lengths within ±0.05 Å of experiment or better for a great variety of solids, surfaces and molecules. However, the following systematic trends are found: (i) most lattice parameters predicted with LDA are too short (figure 2.1), (ii) weak bonds are noticeably too short, for example the Ni-C bond in the Ni carbonyl $Ni(CO)_4$, the bond between two magnesium atoms (which are closed shell systems) and the length of hydrogen bonds such as that in the water dimmer H-O-H---OH_2; (iii) the binding energies calculated with the LDA are typically too large, sometimes by as much as 50% in strongly bound systems and even more in weakly bound materials .Comparison with experiment shows that the

LDA predicts densities, which are mostly too high (bond distances are too short) while the GGA improves the agreement with experiment.

2.3.2. Generalized gradient approximation

Gradient-corrected density functionals as suggested by Perdew [58], Becke [59], Perdew and Wang [60] and Perdew, Burke and Ernzerhof [61] offer a remedy to the LDA discussed above. The basic idea in these schemes is the inclusion of terms in the exchange-correlation expressions that depend on the gradient of the electron density and not only on its value at each point in space. Therefore, these corrections are also sometimes referred to as "non-local" potentials. As example, Table 2.1 gives the form suggested by Becke (1988) for the exchange part and Perdew (1986) for the correlation. Energies are given in Hartree atomic units; the units for the electron and spin densities are number of electrons / (Bohr radius)^3. The constant b in Becke's formula is a parameter fitted to the exchange energy of inert gases. The explicit form of the functions f and g in Perdew's expression for the correlation energy is given in the original paper by Perdew [59].

While dissociation energies calculated with these corrections rival in accuracy the best post-Hartree-Fock quantum chemistry methods, gradient corrected density functional calculations are computationally much less demanding and more general. Gradient corrected density functionals have been studied extensively for molecular systems, for example by Andzelm and Wimmer [62].The results are very encouraging and this

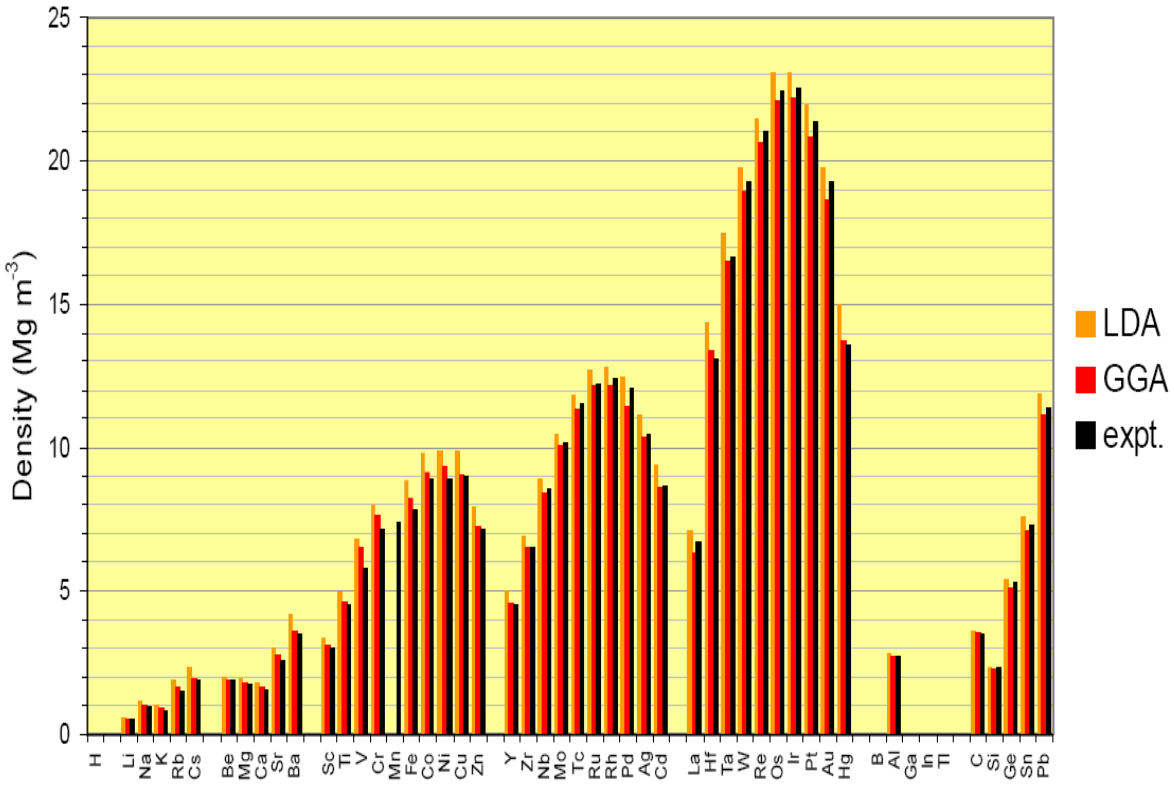

Figure 2-1. Density of selected elements computed with the local density approximation (LDA) and the generalized gradient approximation (GGA).

.

Table 2-1. Gradient-correction to the total energy for exchange by Becke [52] and correlation by Perdew [58].

	$E_{GGA} = E_{LSD} + E_x^G + E_c^G$
Becke (1988) Gradient-corrected exchange	$E_x^G = b\sum_\sigma \int \frac{\rho_\sigma x^2{}_\sigma}{1+6bx_\sigma \sinh^{-1} x_\sigma} dr$ $x_\sigma = \frac{\lvert\nabla\rho\rvert}{\rho_\sigma^{4/3}} \qquad \sigma = \uparrow or \downarrow$
Perdew (1986) Gradient-corrected correction	$E_c^G = \int f\left(\rho_\uparrow, \rho_\downarrow\right) e^{-g(\rho)\lvert\nabla\rho\rvert} \lvert\nabla\rho\rvert^2 dr$

approach could turn out to be of great value in providing quantitative thermochemical data. The one-particle eigenvalues obtained from gradient-corrected exchange-correlation potentials are not significantly different from the LDA eigenvalues. Therefore, these potentials do not (and are not intended to) remove the discrepancy between calculated and measured energy band gaps. Figure 2.1 gives a comparison of LDA and GGA with experiments. The use of GGA has little influence on local properties and tends to overestimate the bond lengths and cell parameters, but does lead usually to a significant improvement in global changes in the total energy, such as those that result when two atoms combine to make a molecule. In this work, we used the PBE form of the GGA [58], which was designed to be more robust and accurate than the original GGA

formulation [60]. The method used was employed because of its robustness for metallic systems.

2.4. Planewave pseudopotential method

2.4.1. Planewaves and pseudopotentials

Planewaves and pseudopotentials are hallmark of the method and they form a very natural alliance. They are so fundamental that their strength and weakness deserve special attention. In PW pseudopotential method, the model system is constructed in 3D periodic supercell which allows Bloch's theorem to be applied to the electron wavefunctions:

$$\psi_{n,k}(r) = u_{n,k}(r)\exp(ik.r) \tag{2-17}$$

The function $u(r)$ has the periodicity of supercell. It can be of any suitable mathematical form and usually one chooses a series expansion in terms of a set of basis function. In PW pseudopotential, planewaves are used for this expansion, so that each single-electron wavefuntion $\psi_{n,k}$ is written as

$$\psi_{n,k}(r) = \sum u_{n,k}(G)\exp(i(k+G).r) \tag{2-18}$$

The $\mu_{n,k}$ are the expansion coefficients. The wavevectors G' are such that the planewaves are commensurate with the supercell. Both the number of G-vectors in the sum and the number of k's considered should in principle be infinite. The exponential term is a planewaves of wavevector k which must be commensurate with the entire system (i.e. not just the periodically-replicated cell). For an infinite system there is an infinite number of k vectors, at each of which solutions for $\psi_{n,k}$ exist. This simply reflects the fact that

the number of electrons is infinite. However, a great simplification comes about when one realises that the change in $\psi_{n,k}$ with k becomes negligible for k-points that are close together. This means that one may calculate at a finite number of k-points. We speak of this idea as k-point sampling. The set of vectors $\{G\}$, on the other hand, should in principle be infinite to obtain an exact representation of the wavefunction. This is never necessary because summing over a finite number of G's will yield sufficient accuracy. Planewaves basis set has many advantages:

- It is unbiased, so all space is treated the same
- It is complete
- There is a single convergence criterion
- Planewaves are mathematically simple and their derivatives are products in k-space
- Planewaves do not depend on atomic positions

and its disadvantage is that (i) the number of planewaves needed is determined by the greatest curvature of the wavefunction and (ii) empty space has the same quality of representation and cost a regions of interest.

The advantages speak for themselves i.e the first three mean that one can always ensure that the basis set is adequate for a calculation by increasing the number of planewaves until the quantity of interest stops changing. In other words, the quality of the basis set depends on a single parameter, usually expressed as the energy a of free electron whose wavefunction has the same wavevector as the largest wavevector in the planewave basis,

$$E_c = \frac{\hbar^2 (G+k)^2}{2m}. \tag{2-19}$$

All planewaves of 'energy' less than the cutoff energy E_c are used in the expansion. The mathematical simplicity of planewaves means the method is easier to implement, crucially so for the calculation of ionic forces which adds little complexity or cost to the calculation. Equally important in this context is the originless nature of planewaves. Their independence from atomic positions means that the forces do not depend on the basis set—there are no 'Pulay' or 'wavefunction' forces [63]. Even more important, new developments are easiest in planewave codes. An idea to calculate a property is most rapidly realised in a planewave basis and even if other methods catch up in time, the planewave approach remains as the reference. From a computational viewpoint the first of the disadvantages appears to be very serious.

2.4.2. Pseudopotential approximation

The rapid oscillations of the wavefunctions near to the nucleus, due to the very strong potential in the region and the orthogonality condition between different states, mean that a very large cutoff energy and hence basis set, would be necessary. Fortunately, the study of Physics and Chemistry shows that the core electrons on different atoms are almost independent of the environment surrounding the atom and that only the valence electrons participate strongly in interactions between atoms. Thus, the core electron states may be assumed to be fixed and a pseudopotential may be constructed for each atomic species which takes into account the effects of the nucleus and core electrons [64-66].

The pseudopotential approximation allows the electronic wavefunctions to be expanded using a much smaller number of planewave basis states. It is well known that most physical properties of solids are dependent on the valence electrons to a much greater extent than on the core electrons. The pseudopotential approximation exploits this by removing the core electrons and replacing the strong ionic potential by a weaker pseudopotential that acts on a set of pseudo wavefunctions rather than the true valence wavefunctions. An ionic potential, valence wave function and corresponding pseudopotential and pseudo wave function are illustrated in fig. 2.5. The valence wavefunctions oscillate rapidly in the region occupied by the core electrons due to the strong ionic potential in this region. These regions maintain the orthogonality between the core wavefunctions and the valence wavefunctions, which is required in the Pauli's exclusion principle.

The pseudopotential is constructed in such a way that its scattering properties or phase shifts for the pseudo wavefunctions are identical to the scattering properties of the ion and the core electrons for the valence wavefunctions, but in such a way that the pseudo wavefunctions have no radial nodes in the core region. The phase shift produced by the ion core is different for each angular momentum component of the valence wave function and so the scattering from the pseudopotential must be angular momentum dependent. The most general form for pseudopotential is

$$V_{NL} = \sum_{lm} |lm\rangle V_l \langle lm| \tag{2-20}$$

Where $\langle lm|$ are the spherical harmonics and V_l is the pseudopotential for angular momentum l. Acting on the electronic wave function with this operator decomposes the

wave function into the spherical harmonics, each of which is the multiplied by the relevant pseudopotential V_l.

A pseudopotential that uses the same potential for all the angular momentum components of the wave function is called a local pseudopotential. Pseudopotential is a function only of the distance from the nucleus. It is possible to produce arbitrary, predetermined phase shifts for each angular momentum state with a local potential, but there are limits to the amount that the phase shifts can be adjusted for the different angular momentum states, while maintaining the crucial smoothness and weakness of the pseudopotential. Without a smooth, weak pseudopotential it becomes difficult to expand the wavefunctions using a reasonable number of planewaves basis states.

2.5. *k*-sampling

Electronic states are allowed only at a set of k-points determined by the boundary conditions that apply to the bulk solid. The density of allowed k-points is proportional to the volume of the solid. The infinite numbers of electrons in the solid are accounted for by an infinite number of k-points and only a finite number of electronic states are occupied at each k-point.

The Bloch theorem changes the problem of calculating an infinite number of electronic wavefunctions to one of calculating a finite number of k-points. The occupied states at each k-point contribute to the electronic potential in the bulk solid so that in principle an

infinite number of calculations are needed to compute this potential. However the electronic wavefunctions at k-points that are very close are identical. Hence it is possible to represent the electronic wavefunctions over a region of k space by the wavefunctions at the single k-point. In this case the electronic states at only a finite number of k-points are required to calculate the electronic potential and hence determine the total energy of the solid.

Methods have been devised for obtaining very accurate approximations to the electronic potential from a filled electronic band by calculating the electronic wavefunctions at special sets of *k*-points. The two most common methods are those of Chadi and Cohen [66] and Monkhorst and Pack [67]. Using these methods, the electronic potential and the total energy of an insulator can be obtained by calculating the electronic states at a very small number of k-points. A denser set of k-points are required to calculate the electronic potential and the total energy of a metallic system in order to define the Fermi surface precisely.

However, the computational cost of performing a very dense sampling of k space increase linearly with the number of k-points in the Brillouin zone (BZ). Density functional codes approximate these k space integrals with a finite sampling of k-points. Special k-points schemes have been developed to use the fewest possible k-points for a given accuracy, thereby reducing the computational cost. The most commonly used scheme is that of Monkhorst and Pack [67].

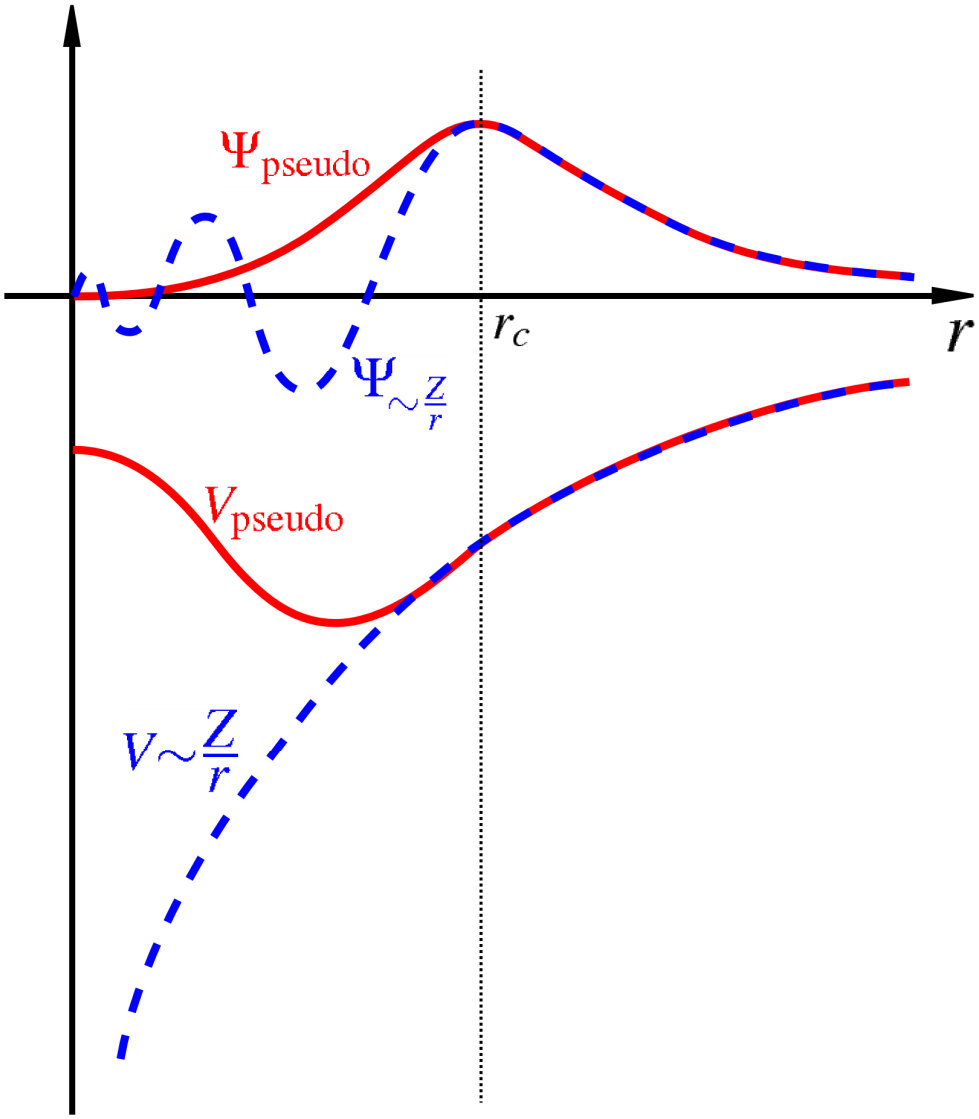

Figure 2-2. Comparison of a wavefunction in the Coulomb potential of the nucleus (blue) to the one in the pseudopotential (red). The real and the pseudowavefunction and potentials match above a certain cutoff radius r_c [66].

2.6. Planewave pseudopotential codes CASTEP and VASP

In this thesis we have employed two planewave pseudopotential codes i.e. CASTEP [68, 69] and VASP [70-72]. In section 2.6.1 and 2.6.2 below we give a brief explanation of the codes. The CASTEP code has been used to determine the equilibrium lattice parameters and the heats of formation for the Ti-Al and the Pt-Ti structures while the VASP code has been used to determine the elastic constants and the phonon dispersions. We have also calculated the density of states using CASTEP and will present all the results calculated in chapter 3 and 4.

2.6.1. CASTEP code

CASTEP is a software package which uses density functional theory with a planewaves basis set to calculate electronic properties of solids from first principles. The CASTEP program is a first principle quantum mechanical (*ab initio*) code for performing electronic structure calculations. Within the density functional formalism it can be used to simulate a wide range of materials including crystalline solids, surfaces, molecules, liquids and amorphous materials; the properties of any material that can be thought of as an assembly of nuclei and electrons can be calculated with the only limitation being the finite speed and memory of the computers being used. CASTEP is a fully featured first principles code and as such its capabilities are numerous. Aiming to calculate any physical property of the system from first principles, the basic quantity is the total energy from which many

other quantities are derived. For example the derivative of total energy with respect to atomic positions results in the forces and the derivative with respect to cell parameters give stresses. These are then used to perform full geometry optimizations and possibly finite temperature molecular dynamics. Furthermore, symmetry and constraints (both internal and external to the cell) can be imposed in the calculations, either as defined by the user, or automatically using in-built symmetry detection.

The total-energy code used, CASTEP, performs a variational solution to the Kohn-Sham equations by using a density mixing scheme [72] to minimize the total energy and also conjugate gradients to relax the ions under the influence of the Hellmann-Feynman forces.

CASTEP uses fast Fourier transforms (FFT) to provide an efficient way of transforming various entities (wavefunctions, potentials) from real to reciprocal space and back as well as to reduce the computational cost and memory requirement for operating with the Hamiltonian on the electronic wavefunctions, a planewave basis for the expansion of the wavefunctions. The convergence of this expansion is controlled by a single parameter, namely the highest frequency at which the series is terminated (conventionally defined as the highest kinetic energy of a planewave).

2.6.2. VASP code

Vienna Ab-initio Simulation Package (VASP) is a package for performing ab-initio quantum-mechanical molecular dynamics (MD) using pseudopotentials and a planewaves

basis set. The approach VASP is based on a finite-temperature local-density approximation (with the free energy as variational quantity) and an exact evaluation of the instantaneous electronic ground state at each MD-step using efficient matrix diagonalization schemes and efficient Pulay mixing. These techniques avoid all problems occurring in the original Car-Parrinello method which is based on simultaneous integration of electronic and ionic equations of motion. The interaction between ions and electrons is described using ultrasoft Vanderbilt pseudopotentials (US-PP) or the projector augmented wave method (PAW) [73]. Both techniques allow a considerable reduction of the necessary number of planewaves per atom for transition metals and first row elements. Forces and stresses can be easily calculated with VASP and used to relax atoms into their instantaneous ground state.

2.7. Heats of formation

The heats of formation of compounds and associated entropies provide the basis for understanding and constructing phase diagrams. Knowledge of these quantities offers the prospect of disentangling which of the observed phases might occur upon varying the means of fabrication. Such modeling of alloy phase behavior is of considerable technological relevance. The heat of formation can be estimated by

$$\Delta H_f = E_c - \sum_i x_i E_i \qquad (2\text{-}21)$$

where E_c is the calculated total energy of the compound, E_i is the calculated total energy of element i in the compound. We will discuss the results of the lattice parameters and heats of formation for Ti-Al and Pt-Ti binary alloys in the next Chapter.

2.8. Elastic properties

2.8.1. Theory of elasticity

From the perspective of materials physics, the elastic constants C_{ij} contain some of the more important information that can be obtained from ground-state total-energy calculations. A given crystal structure cannot exist in a stable or metastable phase unless its elastic constants obey certain relationships. The C_{ij} also determines the response of the crystal to external forces, as characterized by the bulk modulus, shear modulus, Young's modulus and Poisson's ratio and so play an important role in determining the strength of a material [74].

First-principles calculations that use periodic boundary conditions assume the existence of a single crystal, so all elastic constants can be determined by direct computation. The calculated C_{ij} can then be used to check the experimental bulk and shear moduli, if available and to calibrate model calculations. In addition, the elastic constants can be used to check the phase stability of proposed compounds [75, 76]. First-principles calculations can thus be used to predict the existence and properties of new materials and phases.

2.8.2. Definition of elastic constants

To determine the elastic constants of a crystal, a deformation of the unit cell is created by changing the Bravais lattice vectors **R = (a, b, c)** of the undisturbed unit cell to **R′ = (a', b', c')** using a strain matrix **e**

$$R' = R.\begin{pmatrix} 1+e_{xx} & \frac{1}{2}e_{xy} & \frac{1}{2}e_{xz} \\ \frac{1}{2}e_{yx} & 1+e_{yy} & \frac{1}{2}e_{yz} \\ \frac{1}{2}e_{zx} & \frac{1}{2}e_{zy} & 1+e_{zz} \end{pmatrix}. \qquad (2\text{-}22)$$

The deformation leads to a change of the total energy of the crystal

$$U = \frac{E_{tot} - E_0}{V_0} = \frac{1}{2}\sum_{i=1}^{6}\sum_{j=1}^{6} C_{ij} e_i e_j \ , \qquad (2\text{-}33)$$

where E_0 is the total energy of the unstrained lattice, V_0 is the volume of the undistorted cell and the C_{ij} are the elements of the elastic constant matrix with a notation that follows standard convention. Both *i* and *j* run from 1…6 in the sequence {xx, yy, zz, yz, xz, xy}. The tensor of elasticity has 36 elements, the elastic constants, but maximally 21 of these are independent.

2.8.3. Calculation of elastic constants

The simplest case by far is the cubic system where there are only three independent constants, C_{11}, C_{12} and C_{44}. We use this case to illustrate the manner in which the stiffness matrix elements may be determined from strain fields of the form (2-22). If the

applied strain is exx = e with all other ei equal to zero, the energy change is $U = C_{11}e^2/2$. This allows a unique determination of C_{11}. If $e_{yz} = e_{zy} = e/2$, with all other strain components zero, then $U = C_{44}e^2/2$ and we have an independent determination of C_{44}. The bulk modulus, B, is the response to a uniform compression so applying the strain field $e_{xx} = e_{yy} = e_{zz} = e$ allows the computation of B via the relation $U = Be^2/2$. Similarly, the shear modulus can be calculated by using the strain field $e_{zz} = e; e_{xx} = e_{yy} = -e/2$, whereupon $U = 3C'e^2/2$. Finally, the off-diagonal stiffness matrix element C_{12} can be calculated using one or other of the relations

$$B = \frac{1}{2}(C_{11} + 2C_{12}) \qquad (2\text{-}24)$$

$$C' = \frac{1}{2}(C_{11} - C_{12}) \qquad (2\text{-}25)$$

Using both of these relations provides a useful independent check on the accuracy of the computation. A symmetry-general formulation of the calculation of elastic constants from total energy calculations is given by Le Page and Saxe [77].

2.9. Phonons calculations

A detailed knowledge of lattice vibrations is critical for the understanding and quantitative prediction of a wide variety of physical properties of solids. The fundamental thermodynamic functions of internal and free energy, entropy, heat capacity as well as non-linear properties such as thermal expansion and heat conduction are to a considerable extent determined by the vibrations of the constituent atoms in the lattice. Fortunately,

the quantum theory of lattice dynamics is well developed and has proven to be one of the most successful theories of solid state physics.

With the advent of density functional theory and the progress with numerical methods for solving quantum physical equations together with the emergence of more and more powerful computers made it feasible to accurately describe the interatomic interactions in crystals and molecules based on quantum mechanics. Three different techniques for ab initio evaluation of vibrational properties have been developed, namely (i) direct methods based on total energy changes or forces calculated for atoms displaced from their equilibrium position, (ii) analytical calculation of force constants based on a perturbative expansion around the equilibrium geometry and (iii) Fourier transform of the atomic velocity autocorrelation function obtained from a molecular dynamics trajectory [78]. Direct methods (option (i) above) require the evaluation of total energy and forces for the equilibrium geometry as well as of several distorted geometries from which the force constant matrix can be assembled. Phonon dispersion curves along specific high symmetry directions in reciprocal space were determined by the method of interplanar force constants [79], where planes perpendicular to these directions are displaced within an elongated supercell. The most general direct approach to lattice dynamics is based on the ab initio evaluation of forces on all atoms produced by a set of finite displacements of a few atoms within an otherwise perfect crystal. The perfect crystal environment has to be sufficiently large to ensure that interactions of the perturbation with all its translational symmetry equivalent copies are small, which usually requires construction of suitable supercells. The techniques for selecting suitable supercells and atomic displacements,

assembling force constant matrices from the calculated forces and calculating phonon dispersion relations via Fourier transform are well documented [80-82].

2.9.1. Phonon dispersion and polarization vectors

The frequencies $\omega^2(k, j)$ of phonon modes *j* are calculated by diagonalization of the supercell dynamical matrix for each wave vector k along a specified path through the Brillouin zone, thus creating phonon dispersion curves.

$$D(k) \cdot e(k, j)\omega^2(k, j)e(k, j) \tag{2-26}$$

The irreducible representations of all phonon modes at the Γ(0,0,0) point can be calculated, providing in addition Raman and infrared activities of the modes. The complex polarization vectors satisfy the orthonormality relations

$$\sum_j e_i^*(k, j; \mu) \cdot e_l(k, j; v) = \delta_{i,l}\delta_{\mu,v} \tag{2-27a}$$

$$\sum_i \sum_\mu e_i^*(k, j; \mu) \cdot e_i(k, j; \mu) = \delta_{i,j} \tag{2-27b}$$

The polarization vectors $e(k,j;\mu)$ defined for the wave vector *k* centered at the origin of reciprocal space differ from the conventional polarization vector $e(k_\tau,j;\mu)$ as defined for the wave vector kτ pointing from the center of a given Brillouin zone labeled by the reciprocal vector τ. Because of $k = \tau + k_\tau$ the relation between these differently defined polarization vectors is

$$e(k, j; \mu) = e(k, j; \mu)\exp[-2\pi\tau \cdot r_\mu] \tag{2-28}$$

Using the polarization vectors, the displacements caused by a particular phonon and its intensity can be calculated. Assuming amplitude Qk and phase $0 \leq \varphi_k \leq 1$ of the

displacement wave, the displacements $U(n,\mu)$ of atoms (n,μ) for a given wave vector k and phonon branch j are given by the equation

$$U(n,\mu) = \frac{Q_k}{2\sqrt{M_\mu}}\{\mathrm{Re}\, e(k,j;\mu)\cos[2\pi(k\cdot R(n,\mu)-\phi_k)] - \mathrm{Im}\, e(k,j;\mu)\sin[2\pi(k\cdot R(n,\mu)-\phi_k)]\} \tag{2-29}$$

The intensity of phonon modes is obtained from the form factors. The form factor projected on the wave vector is defined as

$$F^{(p)}(k,j) = \frac{1}{k^2}\left|\sum_\mu \frac{k\cdot e(k,j;\mu)}{\sqrt{M_\mu}}\right|^2 . \tag{2-30}$$

However, the intensity of a phonon mode is represented by the simple form factors

$$F^{(s)}(k,j) = \frac{1}{k^2}\left|\sum_\mu \frac{e(k,j;\mu)}{\sqrt{M_\mu}}\right|^2 \tag{2-31}$$

which may be applied to remove unessential phonon branches originating from back folding, or to estimate relative intensities of all modes in varying Brillouin zones.

The MedeA-Phonon module is based on the general direct approach to lattice dynamics and is designed to work independent of a specific underlying code for deriving forces and total energies. However, together with the VASP a fully automatic and highly parallel procedure is provided within MedeA.

2.10. Density of states

The density of states (DOS) is a useful mathematical concept allowing integration with respect to the electron energy to be used instead of the integration over the Brillouin

zone. In addition, the DOS is often used for quick visual analysis of the electronic structure. Characteristics such as the width of the valence band, the energy gap in insulators and the number and intensity of the main features are helpful in qualitatively interpreting experimental spectroscopic data. DOS analysis can also help to understand the changes in electronic structure caused by, for example, external pressure. More accurate methods are based on linear or quadratic interpolations of band energies between the reference points in the Brillouin zone. The most popular and reliable technique, which is based on the tetrahedron interpolation, is unfortunately ill suited to the Monkhorst-Pack grid of special points. Therefore CASTEP uses a simplified linear interpolation scheme [83]. This method is based on the linear interpolation in parallelepipeds formed by the points of the Monkhorst-Pack set, followed by the histogram sampling of the resultant set of band energies.

Chapter 3

Structural properties and heats of formation

In this chapter we discuss the DFT results in particular the lattice constants and the heats of formation of the Ti-Al and Pt-Ti alloys. We further compare the obtained results with the available experimental and theoretical data. Two codes were used to perform calculations; namely CASTEP [69, 70] and VASP [71, 72] as discussed in detail in chapter 2. In the next section we discuss the convergence parameters of the Ti-Al and Pt-Ti alloys.

3.1. Cutoff energy and k-points convergence

3.1.1. Cutoff energy

In order to determine the appropriate cutoff energy for the pure metals (Ti, Al, Pt), single point energy calculations were performed for different kinetic energy cutoffs at default number of k -points for each system within GGA-PBE. The method was employed owing to its robustness for metallic systems. We used ultrasoft pseudopotentials [84], which require significantly less computational resources than the norm-conserving potentials [85]. In figure 3.1 we show the curves of total energy per atom against cutoff energy for the Ti, Al and Pt pure metals. The energy cutoffs of 500 eV, 360 eV and 420 eV were chosen for Ti, Al and Pt, respectively since the energy gave a constant slope at that point

and they yielded energy differences of less than 1meV/atom. The same calculations were done for the $L1_0$ TiAl and B19 PtTi binary alloys and the energy cutoff of 500 eV for the structures were chosen since at this point, the change in energy was negligible. The curves are shown in figure 3.2.

3.1.2. *k*-points

In this section, we show the convergence of the total energies with respect to the k-point sampling set size, as illustrated in figure 3.1. We have carried out total energy calculation at fixed cutoff energy for each structure (determined above) while the number of *k*-points was varied. The total energy with respect to the number of *k*-points was considered converged when the energy change per atom (between two consecutive points) was within 1meV per atom. The k-points were chosen to be 18x18x10, 18x18x18 and 14x14x14 for Ti, Al and Pt respectively as shown in figure 3.1.

The same calculations were done for $L1_0$ TiAl and B19 PtTi structures to determine the *k*-points for the binary alloys. The associated curves are shown in figure 3.2. The *k*-points convergence for the binary alloys were performed using cutoff energy of 500 eV, the *k*-points mesh of 8x8x8 and 8x13x8 was chosen for both $L1_0$ TiAl and B19 PtTi alloys respectively, since the energy difference at this point was found to be less than 1meV. An equivalent number of *k*-points were used for the other binary alloys considered in the current study.

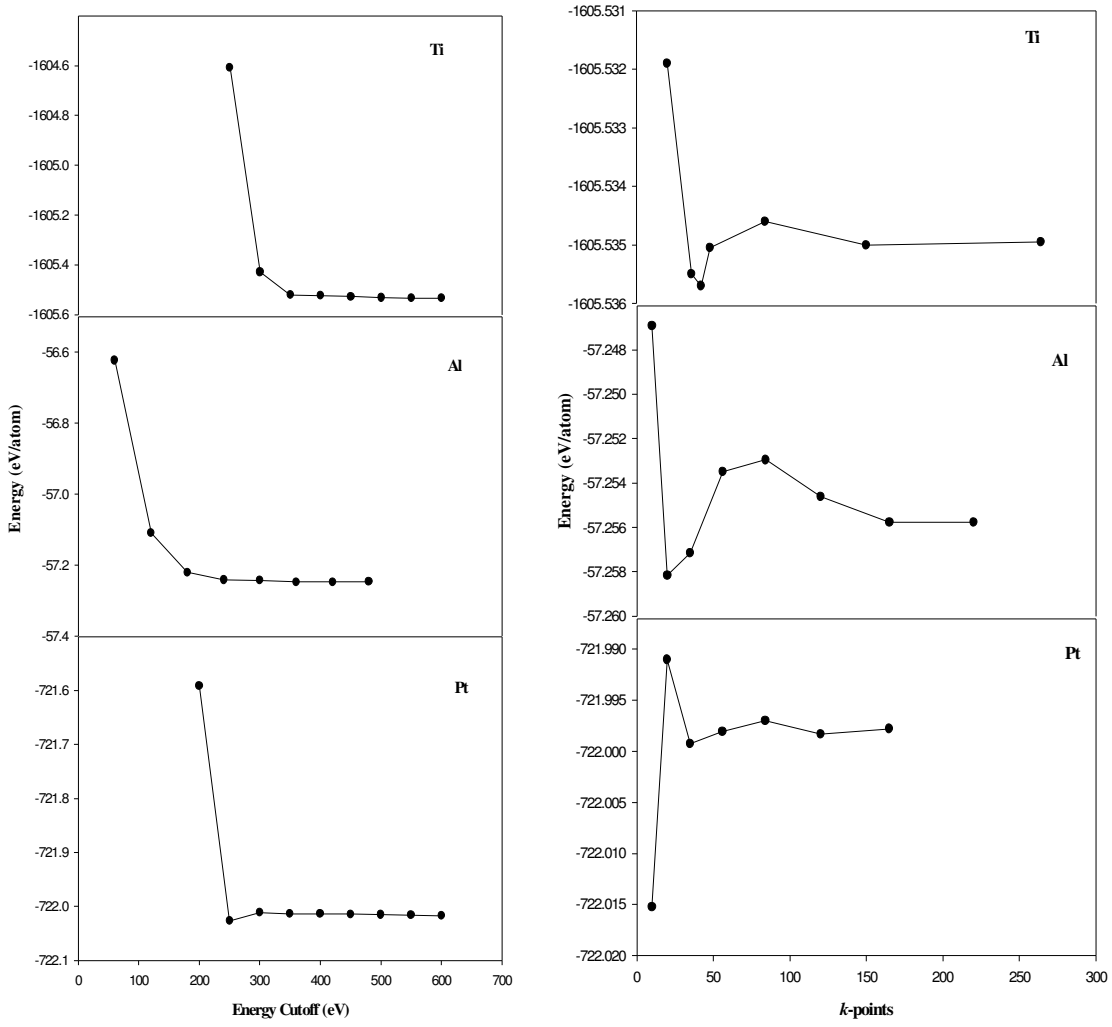

Figure 3-1. The graphs of (a) total energy (eV/atom) against energy cutoff and (b) total energy (eV/atom) against number of k -points for the Ti , Al and Pt.

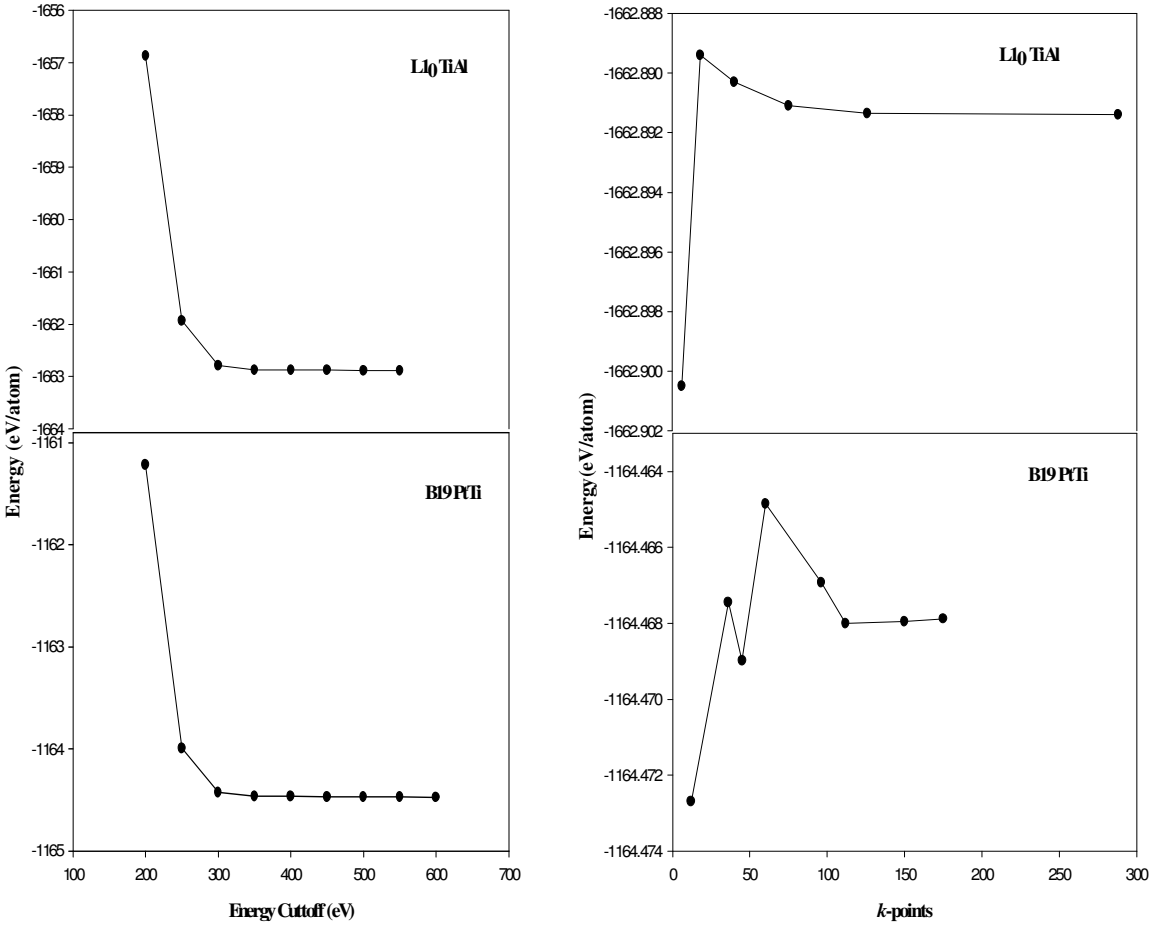

Figure 3-2. The graphs of (a) total energy (eV/atom) against energy cutoff and (b) total energy (eV/atom) against number of k-points for $L1_0$ TiAl and B19 PtTi binary alloys.

3.2. Geometry optimization

The geometry optimization for the Ti-Al and Pt-Ti binary alloys were performed within the generalized gradient approximation using the energy cutoff of 500eV. The lattice parameters of the structures were allowed to vary. The calculations were carried out till a good convergence was obtained. The total energy of the optimized structures was used to calculate the heats of formation which will be discussed in detail in the next section.

3.3. Heats of formation for the Ti-Al and Pt-Ti alloys

3.3.1. Ti-Al

In Table 1 we show the results of the equilibrium lattice constants and the heats of formation. The results of lattice parameters reflect a good agreement with the experimental values (within 3%). The results of the heats of formation are plotted in figure 3.3 of the Ti-Al alloys. The heats of formation have been calculated using both codes (VASP and CASTEP) and are compared with the experiments as well as theoretical data where available. We see that our calculated heats of formation for both codes are in good agreement with the available experimental results. The most stable structure was found to be $L1_0$ with the heat of formation of -0.434 eV. At 75% Ti, DO_{19} was found to be more stable (lowest negative value) than $L1_2$, DO_{22} and DO_3 with the heat of formation of -0.295 eV. There is significant competition between $L1_2$ and DO_{22} Ti_3Al where their formation energy difference is small (ΔH ($L1_2$-DO_{22})= 0.01 eV/atom) for both CASTEP and VASP codes. However, at 25% Ti the formation energy difference

Table 3-1. The equilibrium lattice parameters and heats of formation (ΔH_f) of the Ti-Al alloys

Structure		Lattice Parameters(Å)			ΔH_f (eV/atom)		
		CASTEP	VASP	experimental	CASTEP	VASP	experimental
Ti		a=2.936	2.930	2.945[86]			
		c=4.647	4.635	4.672			
Ti_3Al	$L1_2$	a=4.031	4.038	-	-0.279	-0.264	-0.269[92]
	DO_{22}	a=3.953	3.958	-	-0.269	-0.254	-0.270[93]
		c=8.444	8.447	-			
	DO_{19}	a=5.725	5.728	5.814[87]	-0.295	-0.280	-0.290[93]
		c=4.636	4.646	4.649			
	DO_3	a=6.413	6.422		-0.153	-0.144	
TiAl	$L1_0$	a=3.958	3.975	4.00[88]	-0.434	-0.406	-0.401[94]
		c=4.031	4.083	4.071			
	B32	a=6.321	6.369	-	-0.084	-0.073	-
	B2	a=3.158	3.181	3.185[89]	-0.273	-0.264	-0.260 [95]
$TiAl_3$	DO_3	a=6.413	6.387	-	0.022	0.032	-
	DO_{19}	a=5.489	5.560	-	-0.349	-0.322	-
		c=4.636	4.737	-			
	DO_{22}	a=3.789	3.839	3.847[90]	-0.426	-0.400	-0.366 [94]
		c=8.510	8.623	8.560			
	$L1_2$	a=3.921	3.977	3.980[91]	-0.405	-0.383	-0.400 [93]
Al		a=3.958	4.037	4.032[86]			

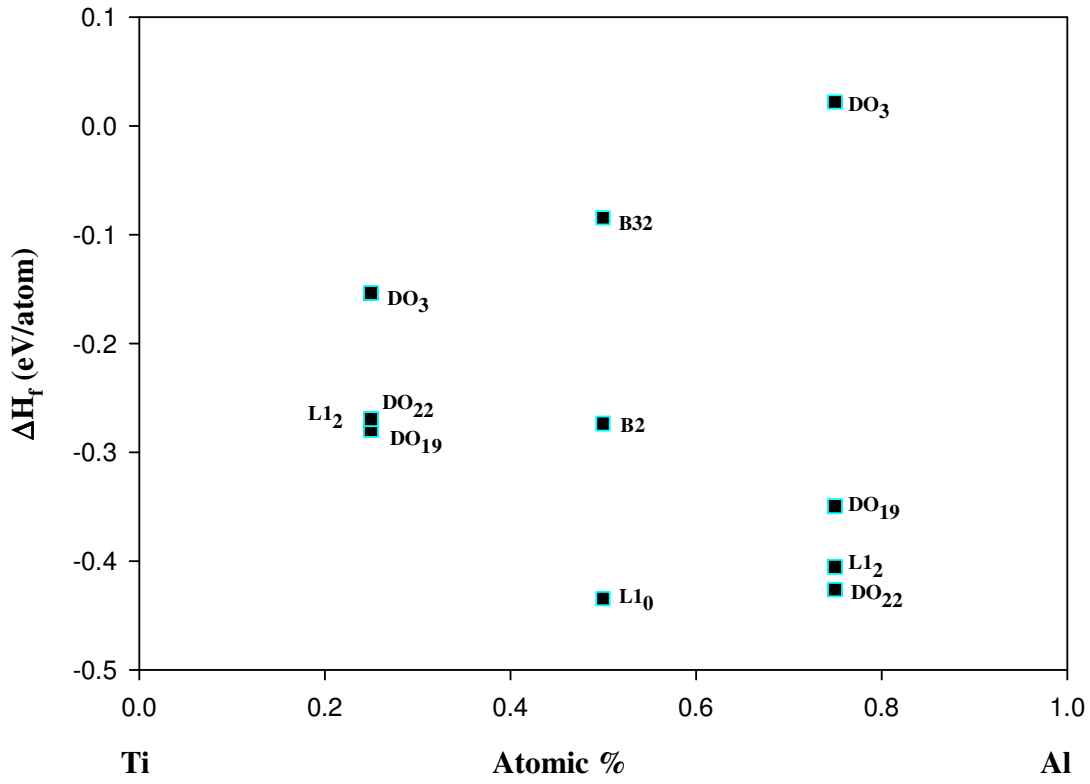

Figure 3-3. Graph of the heats of formation (ΔH_f in eV/atom) against the atomic percentage for the Ti-Al alloys.

is slightly higher (clearly separated). We also note that the B2 phase agrees well with the experimental to within 3%. Furthermore, the Ti_3Al DO_3 phase was found to be highly unstable (with the positive heats of formation) as compared to all the structures.

3.3.2. Pt-Ti

Table 3.2 gives equilibrium lattice constants and heats of formation of Pt-Ti alloys. The results of heats of formation are plotted in figure 3.4. The calculated lattice parameters using CASTEP and VASP codes agree very well and are in accord with available experimental values. The heats of formation from the two codes concur reasonably and are generally well aligned with available experimental values. The most deviation between the codes is 7%, except for the Pt_3Ti, $D0_{24}$ structure whose major difference could partially be ascribed to the absence of relativistic effects in CASTEP.

In our calculations, B19′ PtTi was found to be the most stable structure as compared to other structures with the heat of formation of -0.999eV/atom. Competition is noted between B19′ and B19 as their energy difference is very small. In our calculation, we note that there is no clear distinction between B19 and B19′ using CASTEP where it predicts B19′ to be the most stable structure (by a difference of 1meV/atom). However VASP calculations depicts B19 to be the most stable phase than B19′ phase (ΔH_f (B19′-B19) =0.017eV/atom). However, $L1_0$ seems to be another promising phase which can be

Table 3-2. The equilibrium lattice parameters and heats of formation (ΔH_f) of the Pt-Ti alloys

Structure		Lattice Parameters (Å)			ΔH_f (eV/atom)		
		CASTEP	VASP	experimental	CASTEP	VASP	experimental[96]
Pt_3Ti	DO_3	a=6.301	6.329		-0.527	-0.500	
	DO_{19}	a=5.584	5.617		-0.906	-0.832	
		c=4.508	4.517				
	DO_{22}	a=3.913	3.932		-0.875	-0.822	
		c=7.976	8.007				
	$L1_2$	a=3.932	3.949		-0.918	-0.853	-0.880
	DO_{24}	a=5.569	5.591		-0.920	-0.849	
		c=9.070	9.115				
Pt_8Ti	Dla	a=8.380	8.417		-0.476	-0.453	-0.429
		c=3.934	3.948				
PtTi	B19′	a=4.858	4.873		-0.999	-0.915	
		b=4.608	4.626				
		c=2.769	2.770				
	B19	a= 4.611	4.629	4.55[97]	-0.998	-0.932	-0.827
		b=2.771	2.786	2.73			
		c=4.852	4.873	4.79			
	$L1_0$	a=3.984	3.992		-0.963	-0.911	
		c=3.872	3.901				
	B2	a=3.164	3.180	3.192[97]	-0.821	-0.796	-0.802
	B32	a=6.273	6.300		-0.795	-0.740	
$Pt\ Ti_3$	$L1_2$	a=4.012	4.013		-0.528	-0.490	
	DO_{22}	a=3.798	3.810		-0.523	-0.488	
		c=8.952	8.974				
	DO_{19}	a=5.582	5.598		-0.526	-0.491	
		c=4.804	4.818				
	DO_3	a=6.314	6.334		-0.527	-0.500	
	DO_{24}	a=6.247	5.565		-0.174	-0.481	
		c=7.459	9.626				
	A15	a=5.030	5.043	5.033[98]	-0.689	-0.643	

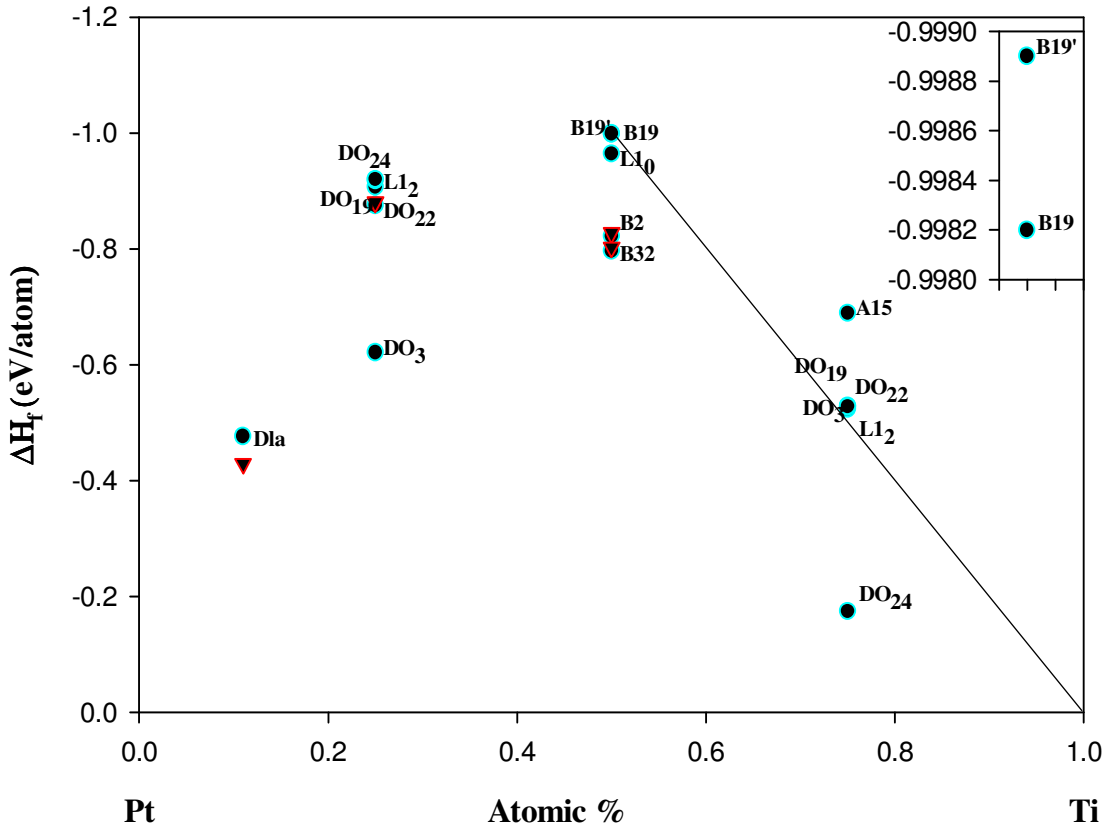

Figure 3-4. Graph of the heats of formation (ΔH_f in eV/atom) against the atomic percentage for Pt-Ti.

used at low temperature transformation, as it appears to be more stable than B2 by 0.142eV/atom. In the $PtTi_3$ composition, A15 phase is more stable than the other phases with the heat of formation of -0.689eV/atom. However DO_{24} is more stable in Pt_3Ti, with the heat of formation less than that of $L1_2$ by 0.002eV/atom, as observed in the graph of heats of formation against atomic percentage. Our results are in good agreement with those of Fernando et al [96]. The values

3.4. Competition between B19, B19', $L1_0$ and B2

The heats of formation calculations, for the 50% PtTi structures, reveal a significant competition between the monoclinic B19′ and the orthorhombic B19 structures where B19/B19' is found to be the most stable structure whereas B2 is the least stable. The results confirm that at low temperature B19/B19' structure is more stable than B2. We also note $L1_0$ is more stable as compared to B2 phase. A comparison of the energy differences between different PtTi phases, yields the relative energies in the order B2>$L1_0$>B19>B19'. The transformation trend is consistent with what has been reported in literature [12, 13, 14]. In Chapter 4 the transformation from B2 to $L1_0$ is clarified since $L1_0$ is found to be more stable than B2.

In summary, our predicted heats of formation results agree well with those found experimentally, in particular, B2 PtTi structure which agrees to within 2% with the experimental values. Moreover, the B2 phase is predicted to be mechanically unstable at low temperature while B19/B19' PtTi was found to be stable. The order in the relative

energies of our results confirms the transformation occurring from B2-B19/B19', as was discussed earlier.

Chapter 4

Mechanical properties, phonon dispersion and density of states of the PtTi

In this chapter we discuss the calculated bulk moduli and elastic constants of the B19′, B19, $L1_0$ and B2 phases of the PtTi 50% composition. We will also present the phonon dispersion and the density of states results of the SMA's.

4.1. Equation of states

The pressures for the 50% composition structures were varied from -5 GPa to 50 GPa using the CASTEP code. The graph of pressure against V/V_0 was plotted and is shown in figure 4.1. The bulk modulus of the B2, $L1_0$, B19 and B19′ structures were determined by fitting the pressure-volume curves to the Birch Murnaghan's equation of states [99]. The results obtained from the graph are shown in Table 4.1 and (in the absence of experimental results) compare well with those obtained from elastic constants using VASP and later also provide calculated shear and Young's moduli of PtTi.

We also present the bulk moduli of the phases that were deduced from the equation of states. A good agreement between the bulk moduli results is noted.

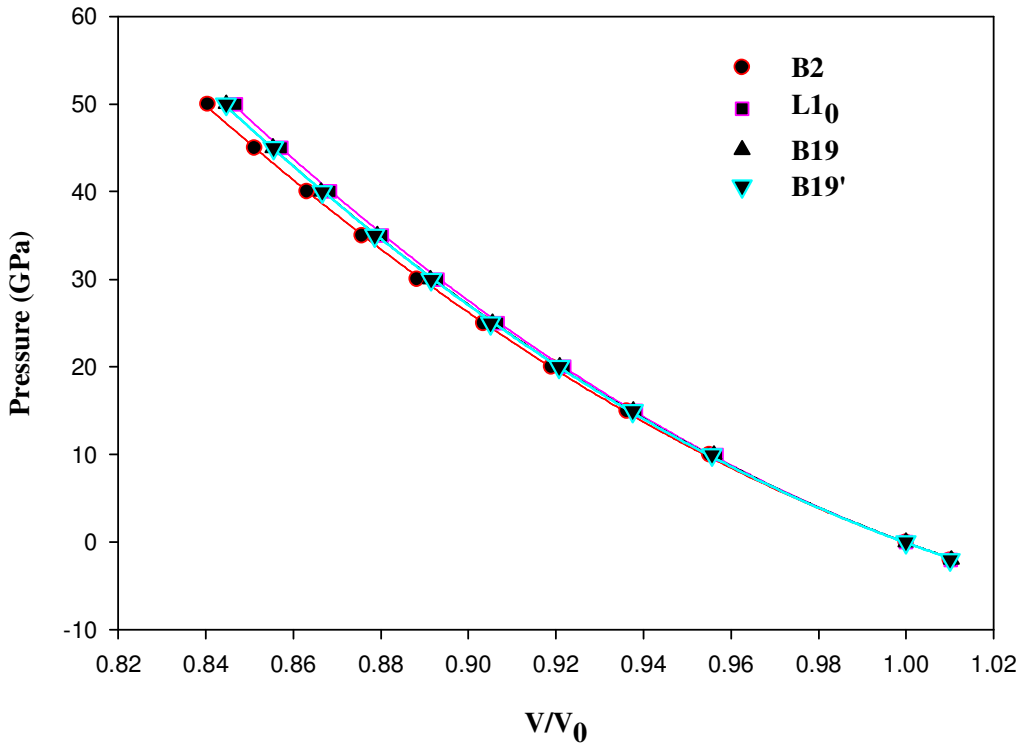

Figure 4-1. The graph of pressure against V/V_0 for the PtTi phases.

Table 4-1. The bulk (B), shear (C'), Young's moduli and the ratio of B to shear moduli for the PtTi structures

Structure	Bulk (EOS)	Shear (C')	Young's	B/C'
B2 PtTi	188 (189)	-32	40	-5.87
$L1_0$ PtTi	202 (201)	40	218	5.26
B19 PtTi	199 (199)	93	145	2.17
B19′ PtTi	201 (201)	85	168	2.38

The structure $L1_0$ appears to be the hardest since it has the highest bulk moduli of elasticity and it is followed by B19′. There is close competition between B19 and B19′ structures in terms of stability and in figure 4.1 respectively P vs V/V_0 are almost overlapping. In Table 4.1, the bulk modulus of B19′ is higher than that of B19 and this also applies to the shear and Young's moduli. The B2 structure appears to be more compressible and easily breakable as suggested by its relatively low moduli. This confirms the results of the heats of formation and the stability trend of our calculations.

The Young's moduli of the 50% structures are shown in Table 4.1 with $L1_0$ having the highest value. B2 has the lowest value of Young's modulus as compared to other structures which indicates its weakness stiffness. Furthermore, we calculated the quotient of bulk modulus to shear modulus, B/C' as to investigate the extent of fracture range in this structures. In Table 4.1, the $L1_0$ structures is more ductile than B19 and B19′ with the highest value of B/C' (5.26). B19 and B19′ structures are more ductile as compared to B2

structures with the B/C' of 2.17 and 2.38 respectively. B2 structure is brittle with the lowest value of -5.87.

4.2. Elastic properties

The stability against small deformations can be studied by considering the elastic constants. The calculated elastic constants of PtTi structures are listed in Table 4.2. The cubic structure B2 is known to be stable at the high temperature while the orthorhombic structure B19 is stable at low temperature. For a cubic material, it is well known that B, C' and C_{44} must be positive for a structure to remain mechanically stable. However, the calculated value of C' is negative, thus indicating the instability of the B2 with respect to the tetragonal distortions. This can be observed from results of our calculations shown in Table 4.2, where B2 structure is unstable as depicted by the heats of formation. It has the lowest bulk moduli as observed in Table 4.1, the small but positive C_{44} and the negative shear moduli. The negative shear modulus of the B2 structure is due to its instability at low temperature. $L1_0$ structure is stable with the positive C_{44} and shear modulus.

The calculated A3 of $L1_0$ structure is approaching unity ($A \approx 1$) which indicates that the structure becomes isotropic and the gap between the bounds vanishes. B19 and B19′ phases are stable with both C_{44} and shear moduli being positive. This as predicted by the graph in figure 4.1, agrees with the heats of formation. There is a good agreement in the heats of formation, bulk moduli and the elastic constants as they predict the same stability trend. Our calculations were done at 0K temperature.

Table 4-2. The elastic constants (GPa) and anisotropic ratios for PtTi structures.

	B19	B19'	$L1_0$	B2
C_{11}	319	320	254	145
C_{12}	133	150	175	210
C_{13}	152	112	158	
C_{33}	317	372	329	
C_{66}	65	58	97	
B	199	201	201	188
C'	93	85	40	-32
C_{44}	59	65	101	45
$A=2C_{44}/(C_{11}-C_{12})$				-1.38
$A1=2C_{66}/(C_{11}-C_{12})$	0.69	0.68	2.42	
$A2=2C_{44}/(C_{11}+C_{33}-2C_{13})$	0.71	1.80	1.51	
$A3=C_{44}/C_{66}$	0.91	1.12	1.04	

4.3. Bain's transformation

If a crystal undergoes a transition from one structure into another, individual atoms in the unit cell or complete atomic planes in the whole crystal must move to new positions in an orderly fashion. This has been known since 1924 when Bain [100] described the martensitic phase transition by a continuous displacement of one or more atoms per unit cell. From his work, on quenched steel, he found an orientational relationship between the austenitic and the martensitic phases, namely that the [001] plane of both the bcc and fcc structures remain unchanged during the transition. Bain described this transition between the bcc and fcc structure via a tetragonal distortion. Both the fcc and bcc lattices can be described as special cases of a body centred tetragonal (bct) unit cell. In the fcc case a and b are equal and the lattice vector c has the length $a\sqrt{2}$, while in the bcc case all three lattice vectors have equal length a'.

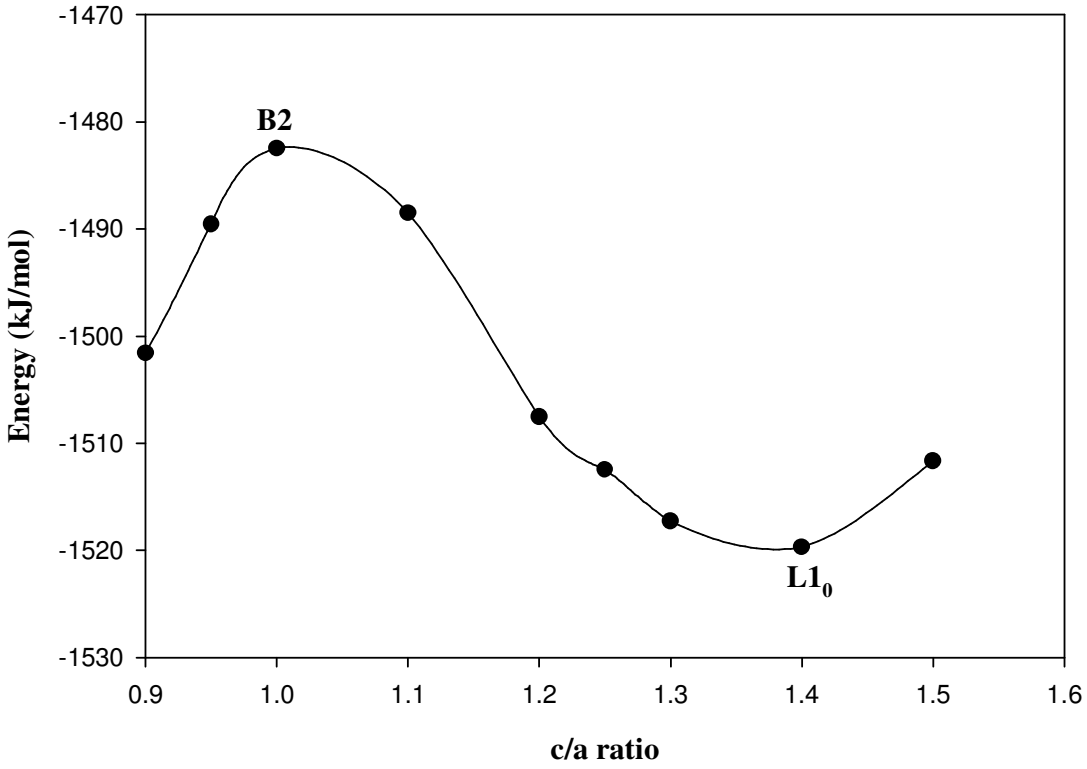

Figure 4-2. Bain's transformation curve from B2 to $L1_0$ PtTi.

The Bain transformation between the fcc and the bcc lattice is thus described by the continuous change of a single variable, namely the *c/a* ratio, so that *c/a*=√ 2 refers to the fcc and *c/a*=1 to the bcc structure.In figure 4.2 we show a curve of the energy versus *c/a* ratio for the B2 structure of PtTi. We varied the c/a ratio and kept the volume constant. In this manner we can deform the B2 structure continuously to a $L1_0$ structure. If we regard B2 structure as a bcc structure with two elements, then the $L1_0$ structure may be regarded as a face centred tetragonal (fct) with two constituent elements. It is observed that the B2 structure is unstable in energy against distortion and $L1_0$ is stable, consequently B2 (bcc) transformed to $L1_0$.

4.4. Phonon dispersions for the B2, $L1_0$, B19 and B19' PtTi

We have also performed the calculations on the phonon dispersion on the 50% composition structures. As has been seen in the heats of formation and elastic properties, our phonon dispersion calculations (figure 4.3) show that indeed B2 structure is unstable since there are soft modes observed in the phonon calculations. The soft modes are observed along M and R directions. The negative slope of the acoustic Γ-M branch corresponds to a pure elastic instability ($C'=1/2(C_{11}-C_{12}) <0$). We observed that the soft modes on the B2 structure are due to the calculated negative shear moduli, which show instability of the structure at low temperature. This can also be observed from the anisotropy factor shown in Table 4.2, where the ratio of B2 is negative.

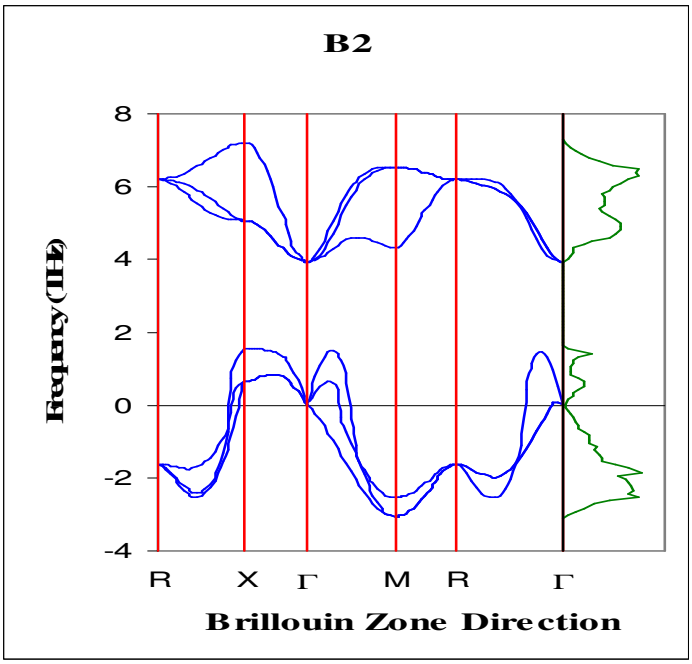

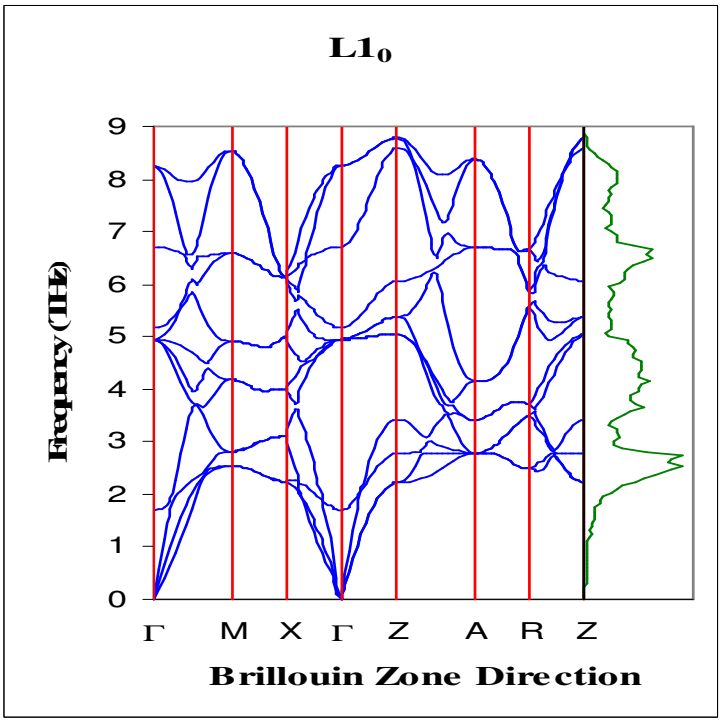

Figure 4-3. The phonon dispersion of the B2 and $L1_0$ PtTi structures

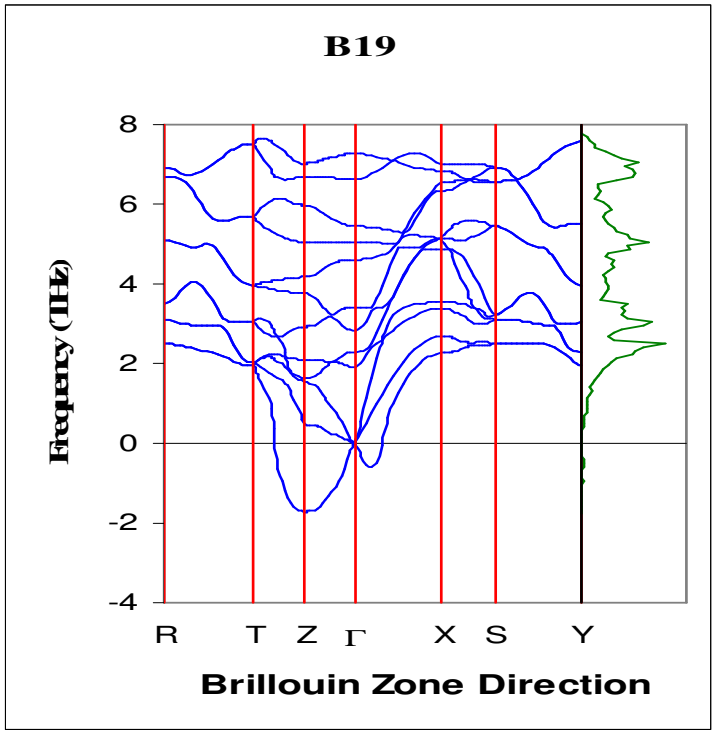

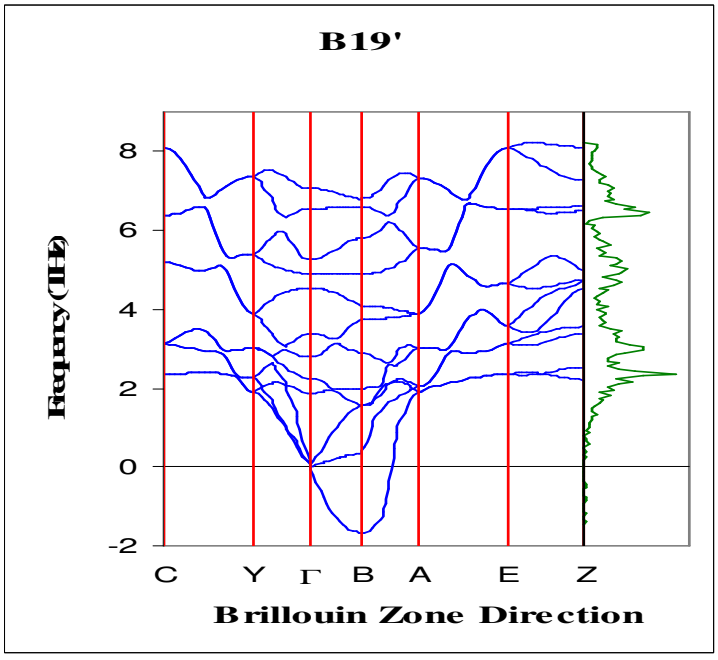

Figure 4-4. The phonon dispersion of the B19 and B19′ PtTi structures

.

$L1_0$, due to the positive C' and C_{44}, can be regarded stable as there are no soft modes observed in its phonon dispersion. The heats of formation and the Bain's transformation predict $L1_0$ structure to be less in energy as compared to B2, suggesting that $L1_0$ is mechanically stable. The same trend is seen on the phonon dispersion curves. There are imaginary soft modes observed in the phonon dispersion curve of the B19/B19′ along Z and B directions respectively. It can be observed from the curves in figure 4.4 that the B19/B19′ is stable as compared to B2 structure. The imaginary modes observed on the B19/B19′ structures don't imply the instability of the structures as proven by the heats of formation and the elastic constants.

4.5. Density of states for PtTi

Structural instabilities in metals are typically related to details of the Fermi surface. In order to better examine the differences in electronic structures of different crystal structures, we plot their density of states (DOS). The DOS is expressed in the number of states per atom per energy interval. We plot the DOS of PtTi composition in the B2, $L1_0$, B19 and B19′ crystal structures in order to compare their phase stabilities.

The total DOS and the PDOS (partial density of states) of the B2 structure shown in figure 4.5 consist of two sets of peaks separated by a dip or pseudogap. The lower energy side is occupied by the sets of peaks coming mainly from Pt *d* states and the higher energy peaks are predominantly due to the *d* states of Ti. The Fermi level E_f lies in a small dip in a rising part of the total DOS below the higher energy peaks which are

mostly unoccupied. The peak at the E_f emanates from contributions of both Pt *d* and Ti *d* with the latter being slightly dominant.

The figures 4.6 and 4.7 show the DOS and PDOS of the B19 and B19′ structures respectively. The PDOS indicate that the Pt *d* states contribute mainly to the lower energy (bonding states) whilst the Ti states contributes mainly to the higher energy (anti-bonding states). The *s* and *p* orbital contributions are negligible since they play a little role in the bonding except to donate some electrons to the Ti *d* states. The DOS peaks of the low temperature phases tend to be broader than the B2 structure, mainly because of the lowering of the symmetry.

In the B19 and B19′ structures the pseudogap dividing contributions of the Pt and Ti *d* states is shallower as compared to B2. Furthermore, the Pt *d* states seem to drop early (at lower energy) and sharply in the case of B19 than in B2 wherein the drop is gradual. In addition the Ti *d* states rises gradually below E_f in B19 as compared to abrupt sharp rise at E_f in B2. Lastly the peak intercepted by $E_{f,}$ in the B19 and B19′ structures, emanates mainly from the Ti *d* states, unlike in B2 where both Pt and Ti *d* states have a noticeable contribution to the peak.

In addition to the B2, B19 and B19' structures, we also show in figure 4.8 for comparison the DOS of the $L1_0$ structure that we have calculated. Similarly to B2, B19 and B19', the DOS for $L1_0$ are also divided by two sets of peaks.

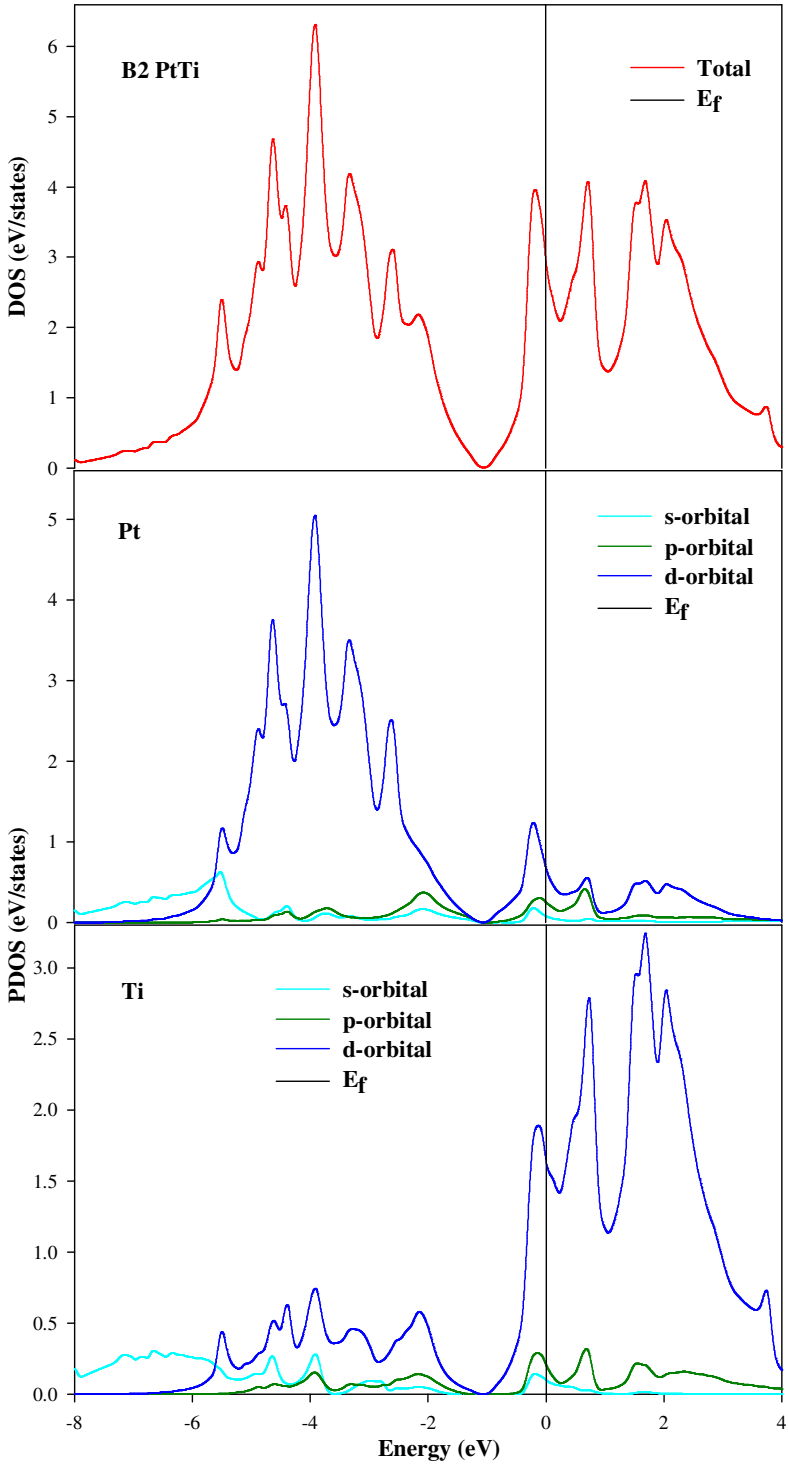

Figure 4-5. Total and partial density of states for B2 PtTi structure.

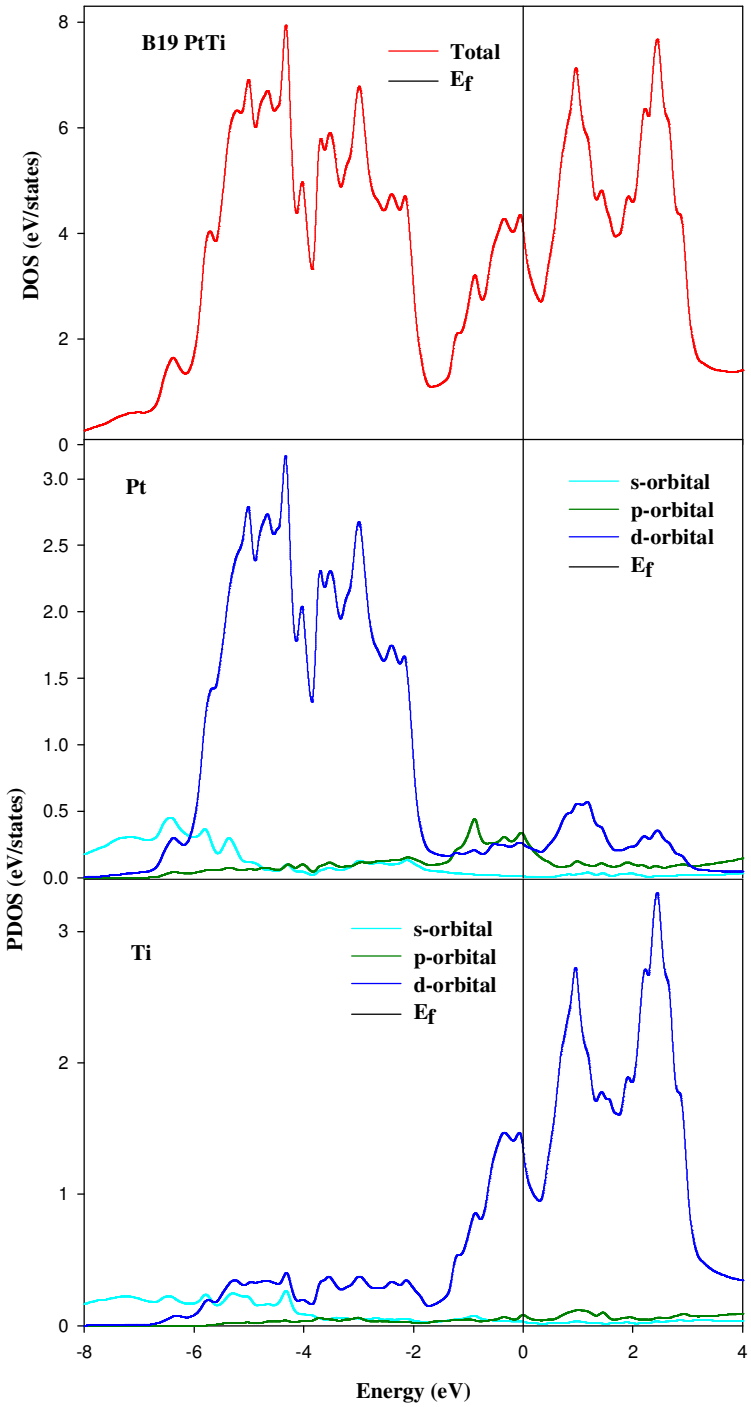

Figure 4-6. Total and partial density of states for B19 PtTi structure.

The lower energy peaks are mainly due to the Pt *d* states and the higher energy peaks to the Ti *d* states. There is also depreciation of density of states at lower energies below the Fermi E_f which results in a broader pseudogap.

The E_f hits the DOS at the shoulder of the dropping peak contributed mainly by the Ti *d* states, as can be clearly seen in the Ti PDOS, in a similar way to B19 and B19' and in contrast to B2. It is conspicuous that $L1_0$ is more stable than the B2 structure, since it has lower number of DOS at Fermi level.

Comparing the DOS of the structures, we found that while the DOS for the B2 structure are quite different from the $L1_0$ structure, the DOS for the B19 and B19′ structures are rather similar to that of the $L1_0$ structure. Furthermore, due to the similarities observed in these three structures, we superimposed their total density of states to investigate their stabilities.

In figure 4.9 we show the superimposed plots of B19 and B19' and the DOS look very similar. The same was done for the B19, B19' and $L1_0$ structures in figure 4.10 and there is a clear distinction between the plots. However, their density of states behaviour at E_f is significant and can be used to correlate their stability. It is also known from literature that the DOS of structures of the same composition can be used to mimic the stability trend with respect to their behaviour at the E_f.

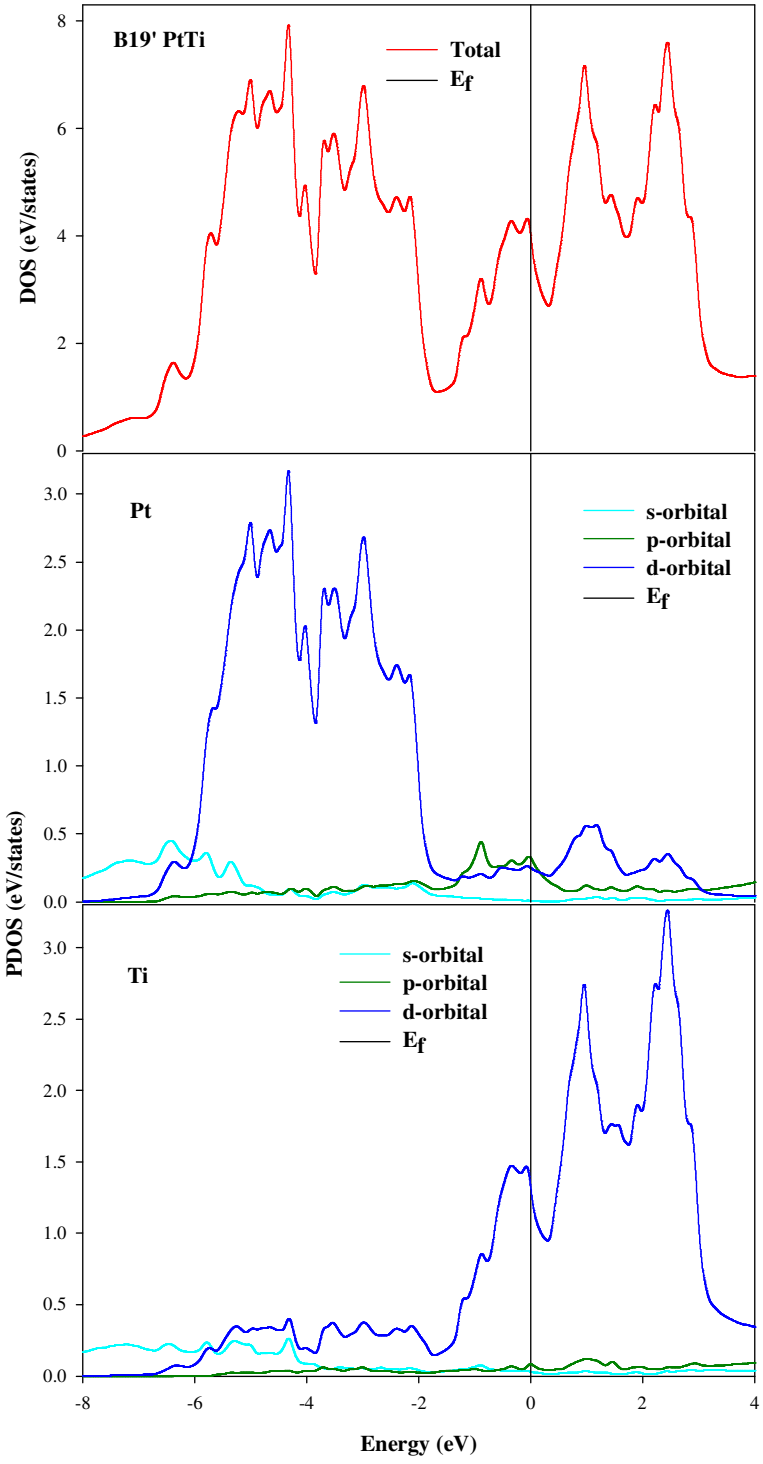

Figure 4-7. Total and partial density of states for B19′ PtTi structure.

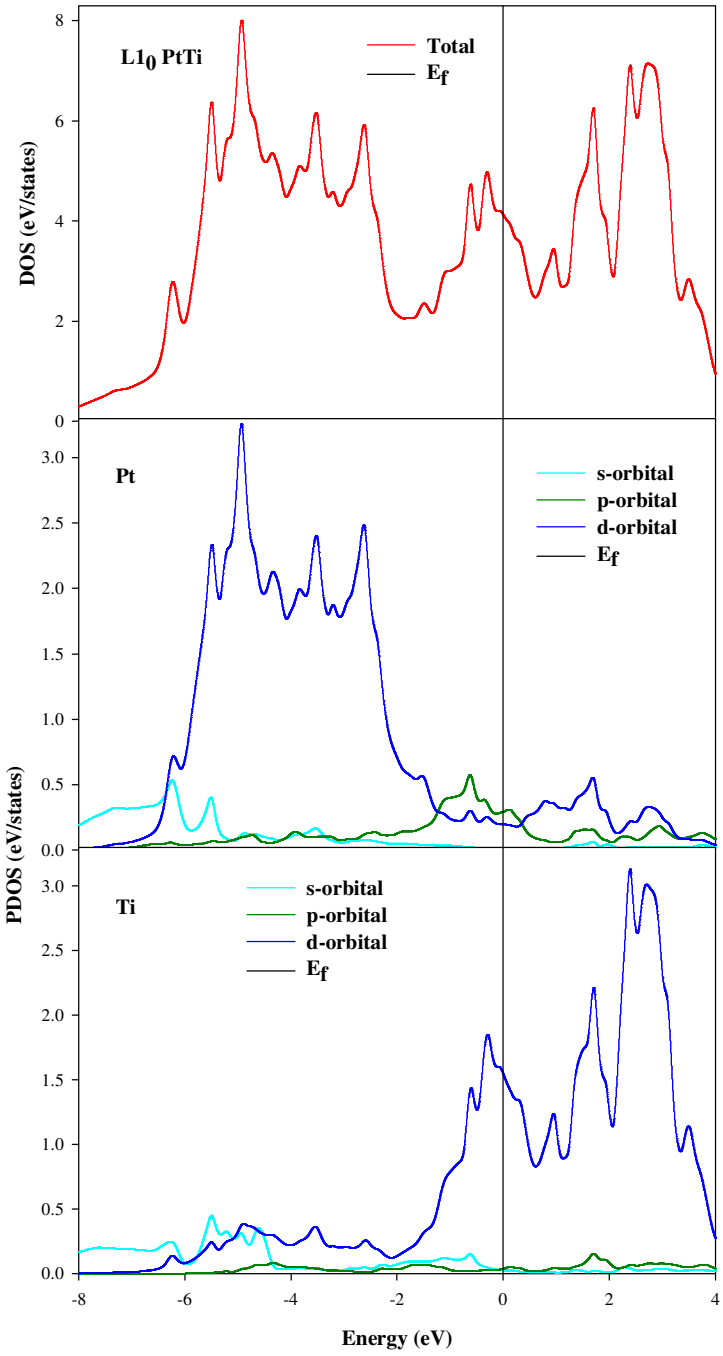

Figure 4-8. Total and partial density of states for $L1_0$ PtTi structure.

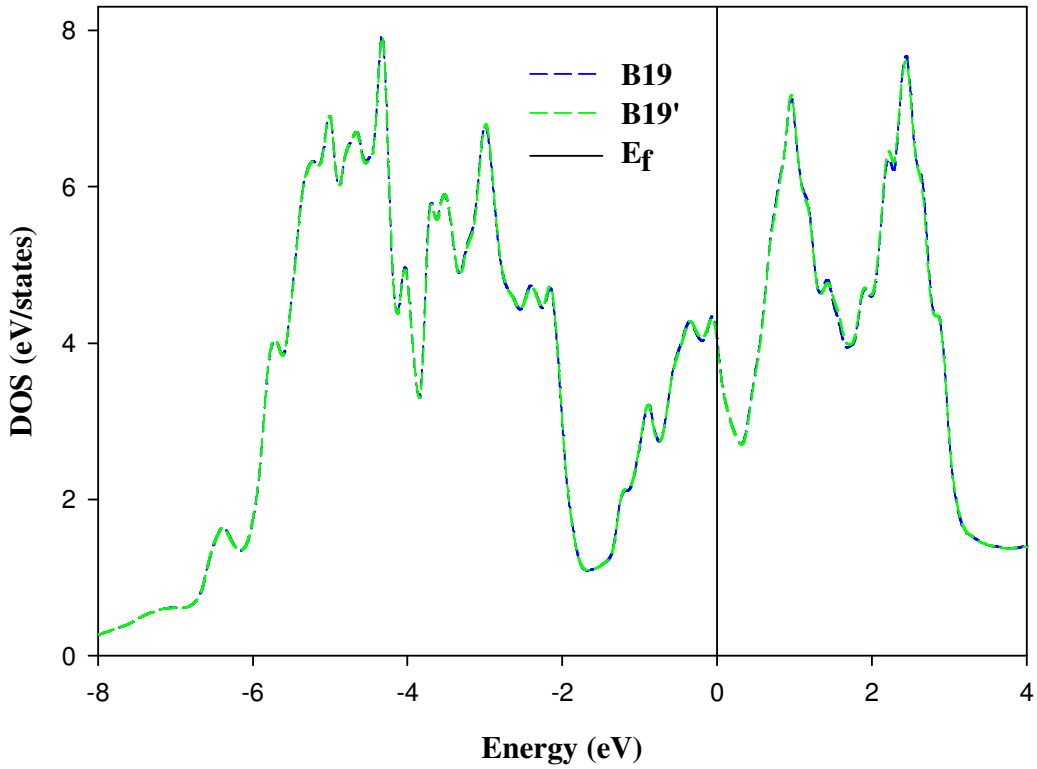

Figure 4-9. The comparison of the total density of states (DOS) for the B19 and B19' PtTi structures.

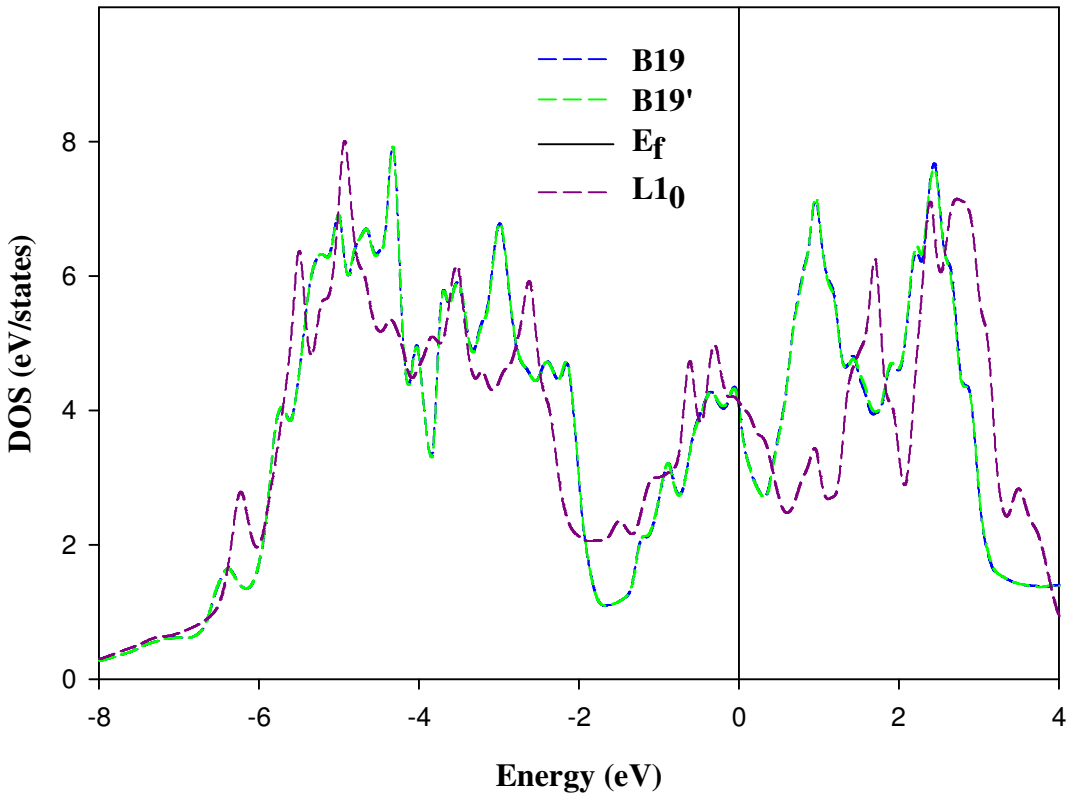

Figure 4-10. Comparison of the total density of states (DOS) for the B19, B19' and $L1_0$ PtTi structures.

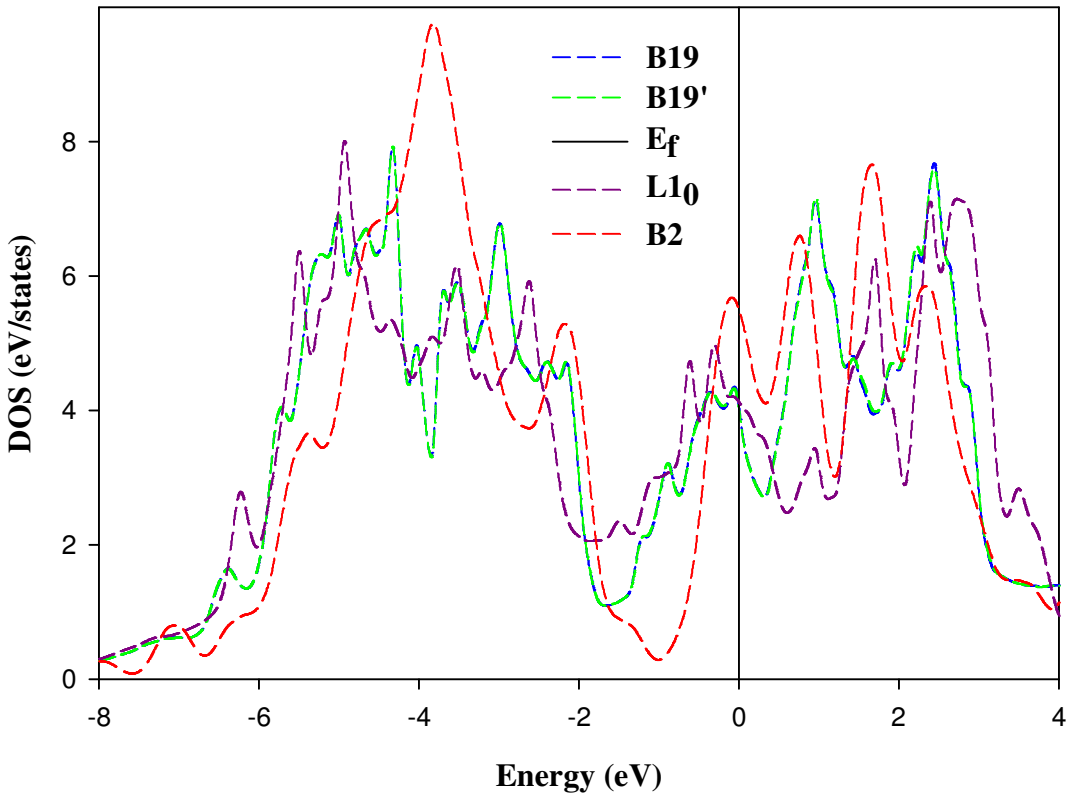

Figure 4-11. Comparison of the total density of states (DOS) for the B19, B19', $L1_0$ and B2 PtTi structures.

The structure with the highest and lowest density of density at E_f is considered the least and most stable, respectively [22]. We note that near E_f the DOS peak of $L1_0$ is much broader compared to the sharp peak observed for the case of B19/B19'. More importantly, it is clearly visible that B19/B19' is more stable than $L1_0$ since it has a lower number of density of states near the Fermi level.

In figure 4.11 we present the superimposed graphs of B19, B19′, $L1_0$ and B2 structures. B2 has the highest number of density of states at E_f as compared to the other structures which confirms that it is the least stable. Our density of states analysis are consistent with the stability trend as predicted by the heats of formation, elastic constants and the phonon dispersion discussed above. This is also in agreement with the experimental observation of the B19/B19' structures which are stable at low temperature whilst B2 is less stable [16]. Our stability trend is then written as B19'> B19> $L1_0$> B2, which is also confirmed by the results on the heats of formation.

Chapter 5

Summary and conclusion

The equilibrium lattice parameters of the Ti-Al and Pt-Ti alloys were performed within the generalised gradient approximations. The results were found to be in good agreement with the available experimental values. We have also investigated the stability of the alloys in particular the 50% composition of the PtTi and the B19/B19′ structures were found to be more stable than the high temperature structure B2. We have also performed the electronic and elastic properties of the 50% composition and they also confirmed what has been found with respect to the phase diagram. Interestingly, we have found that $L1_0$ is more stable than B2 and it has not been reported in the phase diagrams. Furthermore, the calculations on the phonon dispersion and the density of states were performed and they confirm the stability trend of the 50% composition structure. The phonon dispersion curves of the B2 structure showed the availability of the soft modes which are due to the negative shear modulus of the structure. $L1_0$ was found to be more stable since there were no soft modes observed in the phonon dispersion curves and this is due to the positive C_{44} and shear modulus. The bulk modulus of the 50% PtTi phases were calculated from the curve of V/V_0 and it shows a good agreement with the ones calculated using VASP. The negative shear modulus of B2 PtTi suggests the instability of the structure at 0K. Furthermore, we calculated the quotient of bulk to shear modulus and $L1_0$ was found to be more ductile with the highest value and B2 brittle as compared to the other phases with the lowest value. We also calculated the density of states where B2

phase was found to be less stable compared to the other competing structures. B19/B19′ was found to be more stable with the highest number of DOS at Fermi level which is consistence with the results of the heats of formation.

References

[1]. M. Winter, University of Sheffield and Webelements, Ltd (1993-2007)

[2]. G. Sauthoff, In: J.H. Westbrook,R.L. Fleischer, Intermetallic Coumpounds **1** NY: Wiley; 991 (1994)

[3]. R.W. Intermetallics **6**, 563 (1998)

[4]. Y.W. Kim and D.M. Dimiduk JOM. **43,** 401 (1991)

[5]. Y.W. Kim JOM. **46,** 30 (1994)

[6]. M.H. Yoo, C.L. Fu, ISIJ int. **31,** 1049 (1991)

[7]. A.E. Carlsson, P.J. Meschter, In: J.H. Westbrook, R.L. Fleischer, editors. Intermetallic Compounds **1,** 55 (1994)

[8]. G.B. Olson, Science **277,** 1237 (1997)

[9]. T. Biggs, M.B. Cortie, M.J. Witcomb and L.A. Cornish, Metall. Mater. Trans. A, **32A**, 81 (2001)

[10]. L.M. Schetky, In: Intermetallic Compounds. Principles and Practice, J.H. Westbrook and R.L. Fleischer, eds., John Wiley, Chichester, England **2**, 529 (1995)

[11]. H.C. Donkersloot and J.H.N. Van Vucht., J. Less-Common Met. **20**, 83 (1970)

[12]. P.G. Lindquist, C.M. Wayman, In: T. Duerig, K.N. Melton, D. Stockel and C. Wayman, Editors. Engineering aspects of SMA's.Butterworth-Heinemann; 58 (1990)

[13]. O. Rı´os, R. Noebe, T. Biles, A. Garg, A. Palczer, D. Scheiman, et al. Smart Structures and Materials 2005: Active Materials: Behavior and Mechanics. In: SPIE Conf Proc. **5761**, 376 (2005)

[14]. T. Biggs, Y. Yamabe-Mitaria, T. Hara, S. Miura, H. Hosoda. Mater. Sci. Forum **475-479,** 1987(2005)

[15]. H. Nishimura, T. Hiramatsu, Nippon Kinzoku Gakkaishi **21,** 469 (1957)

[16]. T. Biggs, J. of Alloys and Compounds **375,** 120 (2004)

[17]. J.E. Massad, PhD thesis, North Carolina State University (2003)

[18]. E. Posnjak and R. W. G. Wyckoff, Crystal structure of alkali halogenides, Journal of the Washington Academy of Sciences **12**, 248 (1922)

[19]. L.C. Chang and T.A. Read, Transactions of the American Institute of Mining, Metalllurgical and Petroleum Engineers **189**, 47 (1951)

[20]. K. Chen, T. Yu, Y. Zhang and Z. Peng, Acta Geologica Sinica, 111 (1982)

[21]. M.J. Phasha, MSc dissertation, University of Limpopo (2005)

[22]. H.R. Chauke, PhD Thesis, University of Limpopo (2005)

[23]. P.B. Semalty, J. Alloys Compound **419**, 1 (2006)

[24]. K.L. Ng and Q.P. Sun, Mechanics of Materials **38**, 41 (2005)

[25]. R.G. Hennig, A.E. Carlsson, K.F. Kelton and C.L. Henley, Phys Rev. B**71**, 144103 (2005)

[26]. D. Nguyen-Manh and D.G. Pettifor, Intermetallics **7**, 1095 (1999)

[27]. H. Tanei, N. Nakamura, Y. Kake, H. Ogi, K. Kusakabe and M. Hirao Jpn. J. App. Phys. **47,** 3847 (2008)

[28]. H. Yao, L. Ouyang and W. Ching, J. Am. Ceram. Soc. **90**, 3194 (2007)

[29]. S.F. Pugh, Phil. Mag. **45,** 823 (1954)

[30]. S. Kazanc, S. Ozgen, Physica B **365,** 185 (2005)

[31]. M.T. Yin and M.L. Cohen, Phys. Rev. B **45**, 1004 (1980); Phys. Rev. B **25**, 7403

(1982)

[32]. A. Fascolino, E. Molinari and K. Kunc, J. Phys. **21,** 5087 (1988)

[33]. A.A. Quong and B.M. Klein, Phys. Rev. B **46**, 10734 (1992)

[34]. H.W.L. Alves, J.L.A. Alves, A.M. Santos, L.M.R. Scolfaro and J.R. Leite, Braz. J. Phys. **34**, 678 (2004)

[35]. P. Palacios, P. Wahnon and C. Tablero, Comput. Mat. Science **33**, 118 (2005)

[36]. P. Giannozzi, S. de Gironcoli, P. Pavone and S. Baroni, Phys. Rev. B **43**, 7231 (1991)

[37]. D.A. Stewart, New J. Phys. **10**, 043025 (2008)

[38]. S. Shabalovskaya, A. Narmonev, O. Ivanova and A. Dementjev, Phys. Rev. B **48**, 13296 (1993)

[39]. C.T. Liu, H. Kunsmann, K. Otsuka and M. Wuttig, MRS Symposia Proceedings **246**, 247 (1992)

[40]. M. Rajagopalan and M. Sundareswari, J.of Alloys Compounds **379,** 8(2004)

[41]. S. Ghosh, J. Phys. Condens. Matter **20,** 275208 (2008)

[42]. P. Hohenberg and W. Kohn, Phys. Rev. **136**, B864 (1964)

[43]. W. Kohn and L. J. Sham, Phys. Rev. **140**, A1133 (1965)

[44]. G. Bihlmayer, R. Eibler and A. Neckel, Phys. Rev. **50**, 13113 (1994)

[45]. G. Bihlmayer, R. Eibler and A. Neckel, Philos. Mag. **73**, 511 (1996)

[46]. Y.Y. Ye, C.T. Chan and K.M. Ho, Phys. Rev. B **56**, 3678 (1997)

[47]. M.C. Payne, M.P. Teter, D.C. Allan, T.A. Ariar and J.D. Joannopoulos, Rev. Mod. Phys. **64**, 1045 (1992)

[48]. A. Jayaraman, Rev. Mod. Phys. **55**, 65 (1983)

[49]. L.H. Thomas, Proc. Camb. Phil. Soc. **23**, 542 (1926)

[50]. E. Fermi, Z. Phys. **48**, 73 (1928)

[51]. D.R. Hartree, Proc. Camb. Phil. Soc. **24**, 89 (1928)

[52]. V. Fock, Z. Phys. **61**, 126; ibid. **62**, 795 (1930)

[53]. J.C. Slater, Phys. Rev. **81**, 385 (1951)

[54]. J.C. Slater, Quantum Theory of Molecules and Solids **4**, McGraw-Hill, N.Y (1974)

[55]. L. Hedin and B. I. Lundqvist, J. Phys. C **4**, 2064 (1971)

[56]. L. Hedin and S. Lundqvist, J. Phys. (France) **33**, 73 (1972)

[57]. D.M. Ceperley and B. J. Alder, Phys. Rev. Lett. **45**, 566 (1980)

[58]. J.P. Perdew, Phys. Rev. B **33**, 8822 (1986)

[59]. A. D. Becke, Phys. Rev. A **38**, 3098 (1988)

[60]. J.P. Perdew and Y. Wang, Phys. Rev. B **45**, 13244 (1992)

[61]. J.P. Perdew, K. Burke and M. Ernzerhof, Phys. Rev. Lett. **77**, 3865 (1996)

[62]. J. Andzelm and E. Wimmer, J. Chem. Phys. **96**, 1280 (1992)

[63]. J.C. Philips. Phys. Rev. **112**, 73 (1958)

[64]. M.L. Cohen and V. Heine. Solid State Physics **24**, 250 (1970).

[65]. M. T. Yin and M. L. Cohen, Phys. Rev. B **25**, 7403 (1982).

[66]. D. L. Chadi and M. L. Cohen, Phys. Rev. B **8**, 5747 (1973).

[67]. H.J. Monkhorst and J.D. Pack, Phys. Rev. B **13**, 5188 (1976)

[68]. V. Milman, B. Winkler, J.A. White, C.J. Pickard, M.C. Payne, E.V. Akhmatskaya and R.H. Nobes, Int. J. Quantum Chem, **77**, 895 (2000).

[69]. Cerius 3.0. Quantum Mechanics-Physics. CASTEP, ESOCS, Fast Structure, April 1997, MSI, San Diego, CA.

[70]. G. Kresse, J. Hafner, Phys. Rev. B **47**, 558 (1993); ibid **49**, 14251 (1994)

[71]. G. Kresse, J. Furthmüller, Phys. Rev. B **54**, 11169 (1996); Comput. Mat. Science **6**, 15 (1996)

[72]. G. Kresse, J. Furthmüller and J. Hafner, Phys. Rev. B, **50**, 13181 (1994).

[73]. P.E. Blöchl, Phys. Rev. B **50**, 17953 (1994).

[74]. M.J. Mehl, B.M. Klein and D.A. Papaconstantopoulos, Intermetallic Compounds, Principles. Edited by J.H. Westbrook and R.L. Fleischer, John Wiley & Sons Ltd (1994).

[75]. J. Chen, L.L. Boyer, H. Krakauer and M.J. Mehl, Phys. Rev. B **37**, 3295 (1988)

[76]. M.J. Mehl and L.L. Boyer, Phys. Rev. B **43**, 9498 (1991).

[77]. Y. Le Page and P. Saxe, Phys. Rev. B **63**, 174103 (2001)

[78]. A. Rahman, Phys. Rev. **136**, A 405 (1964)

[79]. K. Kunc and R. M. Martin, Phys. Rev. Lett. **48**, 406 (1982)

[80]. G. Kresse, J. Furthmüller, J. Hafner, Europhys. Lett. **32**, 729 (1995)

[81]. W. Frank, C. Elsässer, M. Fähnle, Phys. Rev. Lett. **74**, 1791 (1995)

[82]. K. Parlinski and Z. Q. Li, Y. Kawazoe, Phys. Rev. Lett. **78**, 4063 (1997)

[83]. G.J. Ackland, Phys. Rev. Lett. **80**, 2233 (1998)

[84]. D. Vanderbilt, Phys. Rev. B **41**, 7892 (1990)

[85]. J.S. Lin, A. Qteish, M.C. Payne and V. Heine, Phys. Rev. B **47**, 4174 (1993).

[86]. S. Ogata, J. Li, N. Hirosaki, Y. Shibutani and S Yip, Phys. Rev. B **70**, 104104 (1993).

[87]. K. Tanaka, T. Ichitsubo, H. Inui, M. Yamaguchi and M. Koiwa, Philos. Mag. Lett. **73**, 71 (1996).

[88]. K. Tanaka, K. Okamoto, H. Inui, Y. Minonishi, M. Yamaguchi and M. Koiwa, Philos. Mag. A **73**, 1475 (1996).

[89]. J. Braun, M Ellner and B. Predel, Z Metallkde, **85**, 855 (1994)

[90]. C.L. Fu, J. Matter. Res. **5**, 971 (1990)

[91]. K. Tanaka, K. Okamoto, H. Inui, Y. Minonishi, M. Yamaguchi and M. Koiwa, Philos. Mag. A **73**, 1475 (1996).

[92]. G. Ghosh, M. Asta, Acta Mater. **53**, 3225 (2005)

[93]. T. Hong, T.J. Watson-Yang, X-Q. Guo, A.J. Freeman, T. Oguchi and Jian-hua Xu, Phys. Rev. B **43**, 1940 (1991)

[94]. O. Kubaschewski, W.A. Dench, Acta Mater. **3,** 339 (1955)

[95]. G.W. Fernando, R.E. Watson and M. Weinert, Phys. Rev. B **58,** 5981 (1998)

[96]. G.W. Fernando, R.E. Watson and M. Weinert, Phys. Rev. B **45,** 8233 (1992)

[97]. H.C. Donkersloot and J.H.N. van Vucht, J. Less.Common. Met. **20**, 83 (1970)

[98]. A.E. Dwight, R. A. Conner, Jr. and J. W. Downey, Acta Crystallogr. **18**, 835 (1965).

[99]. F. Birch, J. Geophys. Res. **83**, 1257 (1978).

[100]. E.C. Bain, Trans. AIME **70**, 25 (1924).

Appendix

Papers presented at conferences

1. Materials Modelling Meeting, held at the University of Limpopo (2007) " First principle study of Ti-Al alloys"
2. South African Institute of Physics conference held at the University of Witwatersrand "ab initio study of Ti-Al alloys"
3. South African Institute of Physics conference held at the University of Limpopo (2008) "Structural and elastic properties of binary PtTi high-temperature shape memory alloys"
4. Advanced Metals Initiative conference held in Gold Reef City (Johannesburg) (2008) "Structural and elastic properties of binary PtTi high-temperature shape memory alloys by ab initio technique"